Review of Scientific Instruments

# Broadband high-energy resolution hard x-ray spectroscopy using transition edge sensors at SPring-8

Cite as: Rev. Sci. Instrum. **92**, 013103 (2021); https://doi.org/10.1063/5.0020642
Submitted: 03 July 2020 . Accepted: 04 December 2020 . Published Online: 12 January 2021

Shinya Yamada, Yuto Ichinohe, Hideyuki Tatsuno, Ryota Hayakawa, Hirotaka Suda, Takaya Ohashi, Yoshitaka Ishisaki, Tomoya Uruga, Oki Sekizawa, Kiyofumi Nitta, Yoshio Takahashi, Takaaki Itai, Hiroki Suga, Makoto Nagasawa, Masato Tanaka, Minako Kurisu, Tadashi Hashimoto, Douglas Bennett, Ed Denison, William Bertrand Doriese, Malcolm Durkin, Joseph Fowler, Galen O'Neil, Kelsey Morgan, Dan Schmidt, Daniel Swetz, Joel Ullom, Leila Vale, Shinji Okada, Takuma Okumura, Toshiyuki Azuma, Toru Tamagawa, Tadaaki Isobe, Satoshi Kohjiro, Hirofumi Noda, Keigo Tanaka, Akimichi Taguchi, Yuki Imai, Kosuke Sato, Tasuku Hayashi, Teruhiko Kashiwabara, and Kohei Sakata

Review of Scientific Instruments ARTICLE scitation.org/journal/rsi

# Broadband high-energy resolution hard x-ray spectroscopy using transition edge sensors at SPring-8

Cite as: Rev. Sci. Instrum. 92, 013103 (2021); doi: 10.1063/5.0020642
Submitted: 3 July 2020 • Accepted: 4 December 2020 •
Published Online: 12 January 2021



Shinya Yamada,[1,a] Yuto Ichinohe,[1] Hideyuki Tatsuno,[2] Ryota Hayakawa,[2] Hirotaka Suda,[2] Takaya Ohashi,[2] Yoshitaka Ishisaki,[2] Tomoya Uruga,[3] Oki Sekizawa,[3] Kiyofumi Nitta,[3] Yoshio Takahashi,[4] Takaaki Itai,[4] Hiroki Suga,[4] Makoto Nagasawa,[4] Masato Tanaka,[4] Minako Kurisu,[5] Tadashi Hashimoto,[6] Douglas Bennett,[7] Ed Denison,[7] William Bertrand Doriese,[7] Malcolm Durkin,[7] Joseph Fowler,[7] Galen O'Neil,[7] Kelsey Morgan,[7] Dan Schmidt,[7] Daniel Swetz,[7] Joel Ullom,[7] Leila Vale,[7] Shinji Okada,[8,b] Takuma Okumura,[9] Toshiyuki Azuma,[9] Toru Tamagawa,[9,c] Tadaaki Isobe,[10] Satoshi Kohjiro,[11] Hirofumi Noda,[12] Keigo Tanaka,[13] Akimichi Taguchi,[13] Yuki Imai,[14] Kosuke Sato,[14] Tasuku Hayashi,[15] Teruhiko Kashiwabara,[16] and Kohei Sakata[17]

## AFFILIATIONS

[1] Department of Physics, Rikkyo University, Toshima-Ku, Tokyo 171-8501, Japan
[2] Department of Physics, Tokyo Metropolitan University, Hachioji, Tokyo 192-0397, Japan
[3] Center for Synchrotron Radiation Research, Japan Synchrotron Radiation Research Institute (JASRI), Sayo, Hyogo 679-5198, Japan
[4] Department of Earth and Planetary Sciences, Graduate School of Science, The University of Tokyo, Bunkyo-Ku, Tokyo 113-0033, Japan
[5] Earth Surface System Research Center, Research Institute for Global Change, Japan Agency for Marine-Earth Science and Technology (JAMSTEC), Yokosuka, Kanagawa 237-0061, Japan
[6] Advanced Science Research Center (ASRC), Japan Atomic Energy Agency (JAEA), Tokai, Ibaraki 319-1184, Japan
[7] Quantum Sensors Group, National Institute of Standards and Technology (NIST), Boulder, Colorado 80305, USA
[8] Engineering Science Laboratory, Chubu University, Kasugai, Aichi 487-8501, Japan
[9] Cluster for Pioneering Research, RIKEN, Wako, Saitama 351-0198, Japan
[10] Nishina Center, RIKEN, Wako, Saitama 351-0198, Japan
[11] Device Technology Research Institute, National Institute of Advanced Industrial Science and Technology (AIST), Tsukuba, Ibaraki 305-8568, Japan
[12] Department of Earth and Space Science, Osaka University, Toyonaka, Osaka 560-0043, Japan
[13] College of Science and Engineering, Kanazawa University, Kakuma-machi, Kanazawa 920-1192, Japan
[14] Department of Physics, Saitama University, Saitama-shi, Saitama 338-8570, Japan
[15] Astromaterials Science Research Group (ASRG), Institute of Space and Astronautical Science (ISAS), Japan Aerospace Exploration Agency (JAXA), Sagamihara, Kanagawa 252-5210, Japan
[16] Submarine Resource Research Center, Research Institute for Marine Resources Utilization, Japan Agency for Marine-Earth Science and Technology (JAMSTEC), Yokosuka, Kanagawa 237-0061, Japan
[17] Center for Global Environmental Research, National Institute for Environmental Studies (NIES), Tsukuba, Ibaraki 305-8506, Japan

[a] **Author to whom correspondence should be addressed:** syamada@rikkyo.ac.jp. **Also at**: Department of Physics, Tokyo Metropolitan University, Hachioji, Tokyo 192-0397, Japan.
[b] **Also at**: Cluster for Pioneering Research, RIKEN, Wako, Saitama 351-0198, Japan.
[c] **Also at**: Nishina Center, RIKEN, Wako, Saitama 351-0198, Japan.

## ABSTRACT

We have succeeded in operating a transition-edge sensor (TES) spectrometer and evaluating its performance at the SPring-8 synchrotron x-ray light source. The TES spectrometer consists of a 240 pixel National Institute of Standards and Technology (NIST) TES system, and 220 pixels are operated simultaneously with an energy resolution of 4 eV at 6 keV at a rate of ~1 c/s pixel$^{-1}$. The tolerance for high count rates is evaluated in terms of energy resolution and live time fraction, leading to an empirical compromise of ~$2 \times 10^3$ c/s (all pixels) with an energy resolution of 5 eV at 6 keV. By utilizing the TES's wideband spectroscopic capability, simultaneous multi-element analysis is demonstrated for a standard sample. We conducted x-ray absorption near-edge structure (XANES) analysis in fluorescence mode using the TES spectrometer. The excellent energy resolution of the TES enabled us to detect weak fluorescence lines from dilute samples and trace elements that have previously been difficult to resolve due to the nearly overlapping emission lines of other dominant elements. The neighboring lines of As K$\alpha$ and Pb L$\alpha$2 of the standard sample were clearly resolved, and the XANES of Pb L$\alpha$2 was obtained. Moreover, the x-ray spectrum from the small amount of Fe in aerosols was distinguished from the spectrum of a blank target, which helps us to understand the targets and the environment. These results are the first important step for the application of high resolution TES-based spectroscopy at hard x-ray synchrotron facilities.


 https://doi.org/10.1063/5.0020642

## I. INTRODUCTION

X-ray absorption (XAS) and x-ray fluorescence (XRF) or x-ray emission spectroscopy (XES) are powerful techniques to measure distribution, chemical state, and local structure of elements. Therefore, they play essential roles in various materials analyses. For example, diagnostics for trace elements are conducted by measuring the energy spectrum of fluorescent x rays. Instruments for performing x-ray spectroscopy are primarily categorized into wavelength-dispersive or energy-dispersive spectrometers. XAS of trace elements has typically been conducted using Si or Ge-based energy-dispersive x-ray detectors. The typical energy resolution of these detectors is about 120 eV in the hard x-ray energy region (>4 keV), which is fundamentally limited by statistical variation of the number of electron–hole pairs created by x-ray photon absorption. However, that resolution is insufficient to fully distinguish the nearly overlapping K and L emission lines of elements in this energy regions (<15 keV), which hinders the ability of trace element analysis to effectively measure natural or otherwise complicated samples. In cases where it is necessary to resolve closely spaced emission lines, a Bent Crystal Laue Analyzer (BCLA) is used in combination with energy-dispersive x-ray detectors.[1] The energy resolution of this system is several tens of eV. However, XES measurements require a high energy resolution, less than 10 eV, and are therefore normally conducted using a wavelength-dispersive bent multi-crystal analyzer spectrometer. The detection efficiency of the BCLA was limited due to narrow acceptance angle and low diffraction efficiency of the analyzer crystals. The analyzer crystals need to be changed depending on the energy region of interest. Recently, multi-crystal spectrometers based on intersecting Rowland circles have been developed and they enhanced the solid angle and the detection efficiency (e.g., Refs. 2 and 3). In such a system, the detectors and the crystals need to be located at a certain distance from the sample, which has a limit to increase the efficiency and the bandpass of the energy range.

These situations demand high-efficiency energy-dispersive x-ray detectors having an energy resolution less than 10 eV. The first technology to deliver this type of performance came in the form of semiconductor type microcalorimeters operating at 50 mK. To achieve a high energy resolution, operating the detectors at such low temperatures is essential since the creation energy of the pairs (e.g., ~eV for electron and hole pairs in semiconductors and ~meV for Cooper pairs in superconductors) and the thermal noise decreases. Recently, the semiconductor type microcalorimeters, such as the Soft X-ray Spectrometer (SXS) on the x-ray astronomical satellite called ASTRO-H (Hitomi),[4] succeeded in solving several issues related to vibration from the cryogenic system[5] and achieved an energy resolution of 4.5 eV at 6 keV in a space environment. Its high energy resolution clearly resolved ionized iron lines and revealed that the hot plasma stored in the galaxy cluster has a low turbulent pressure.[6] Although there is now a great deal of accumulated experience using semi-conductor x-ray microcalorimeters, their high impedance limits the increase in the number of pixels for practical use, and hence, the collection area is fundamentally limited because the heat capacity, and therefore the size, of a single pixel is also limited by its required energy resolution.

A promising alternative candidate is the superconducting transition-edge sensor (TES).[7] Since a way of stabilizing the TES within its narrow transition region was formulated in the mid-1990s,[8] the technical details and physical nature of these devices have been intensively studied, with strong demand from both on-ground and space applications.[9] Thanks to these advances, the TES has been chosen as the detector technology for the future European x-ray observatory called ATHENA,[10] which is planned to have an array of more than 3000 sensors. However, in order to successfully integrate a TES array into other systems in an experiment, the spectrometer design must overcome several difficulties, including suppressing mechanical vibration, isolating electrical interference, shielding against magnetic fields, and synchronizing its timing with other systems. The National Institute of Standards and Technology (NIST) has developed a mature 240-pixel TES spectrometer, which was applied to nuclear physics research at Japan Proton Accelerator Research Complex (J-PARC)[11] and succeeded in measuring fluorescence lines from a Kaonic atom,[12] achieving stable performance even in the challenging environment found at the accelerator. The TES can be applied to a diverse area of scientific problems by changing its design, e.g., thickness or size of TESs and absorbers, to cover a wide range of energies and celestial or terrestrial x-ray sources. For example, the TES can be applied as a particle detector to search for dark matter via inelastic scattering[13] or to measure the mass of neutrinos.[14]

Today, TES x-ray spectrometers are operated for several different applications, e.g., at the Stanford Synchrotron Radiation Lightsource beamline 10-1 (BL 10-1),[15] at the Electron Beam Ion Trap (EBIT) at NIST,[16] for resonant soft x-ray scattering at the Advanced

Photon Source,[17] for particle-induced x-ray emission (PIXE),[18] and for ultrafast time-resolved x-ray emission spectroscopy on a tabletop.[19] However, compared to these applications, which are either targeted at soft x-ray science or tabletop experiments in relatively small laboratories, the potential of TESs for applications at hard x-ray synchrotron facilities has not been explored. Although there were successful reports of using a crystal analyzer system to measure the x-ray absorption fine structure (XAFS) in the hard x ray, it was not ideal for several reasons: crystals were designed for each energy of emission lines and needed precise adjustment each time, the available energy resolution was moderate, and the measurable energy range was narrow.[1] TESs can contribute to the reduction of the alignment time, improve the energy resolution, and expand the energy coverage. Note that although both technologies will progress, the advantage of using TES is that it does not require reflection at the crystals and hence relaxes spatial constraints. Here, we will present the commissioning of a new TES spectrometer at the beamline BL37XU at SPring-8, Japan.[20] The light source of BL37XU can provide hard x-ray photons with an energy range of 4.5 keV–18.8 keV by using first harmonic x rays of the undulator, which is suitable to measure a sample via K$\alpha$ lines from relatively heavy metals and L-lines from rare earth elements. The fluorescence-mode X-ray Absorption Near-Edge Structure (XANES) of dilute elements in various samples was difficult to measure using conventional detectors, such as the Silicon Drift Detector (SDD). Here, we obtain the XANES signal of a dilute aerosol sample that did not work well with the SDD detector. In this paper, we present in detail the setup and data processing procedure, performance of each pixel of the TES, and its application to the simultaneous multi-element analysis of XANES of heavy elements and dilute samples.

## II. EXPERIMENTS

### A. Detector setup

A quasi-monochromatic x-ray beam emitted from the SPring-8 standard undulator (period = 3.2 cm and $B_{max}$ = 0.78 T) was monochromatized to a certain energy (5 keV–37 keV) using a Si(111) monochromator. BL37XU is a hard x-ray undulator beamline in Spring-8 that is mainly used for studies of x-ray micro-/nano-spectrochemical analysis such as XRF/XAFS imaging, wavelength-dispersive XAFS, depth-resolved XAFS, and XRF holography. The flow of the incoming x rays in the BL32XU is shown in Fig. 1(a). Two horizontal deflecting mirrors are placed downstream of the monochromator in order to eliminate higher harmonics and to obtain a focused x-ray beam in the horizontal direction. There are several slits with mechanically movable remote motors, which can reduce the intensity of the beam. The relative energy resolution of the incident x-ray beam, $\Delta E/E$, is ~$2 \times 10^{-4}$, which is proportional to $\sqrt{\sigma_{crystal}^2 + \sigma_{beam}^2}$, where $\sigma_{crystal}$ is the Darwin width of the monochromator crystal (e.g., 20 $\mu$rad–60 $\mu$rad at 14 keV–5 keV) and $\sigma_{beam}$ is an angular divergence of incident x-ray beam (e.g., 5 $\mu$rad with a slit width of 200 $\mu$m and 40 m away from the source). Thus, the effect of operating the slits on the energy resolution of the incident x-ray beam could be at most 3%, ~0.04 eV at 6 keV. Samples and the x-ray windows on the sample side used for both the SDD and TES spectrometer are exposed to ambient air at room temperature.

Since a TES makes use of a thermal process as a measure of photon energy, the speed of the relaxation of the heat deposited in the x-ray absorber limits the response time. In general, this type of detector is difficult to tune to work as fast as an SDD that works by electromagnetic interaction. We used several slits along the beamline to suppress the beam intensity. The vacuum jacket of the cryostat or the Dewar, whose size is 33 × 22 × 66 cm$^3$, is mounted on a movable support structure. This flexibility enables us to tune the x-ray intensity by two orders of magnitude. The setup is presented in Fig. 1. The sample was set at 45° with respect to the incident x ray. The fluorescence that escapes from the surface of the sample is transmitted to the TES array. Since the SDD has a larger effective area, it is positioned to receive photons from the backside of the sample. Two ion chambers are used for the measurement

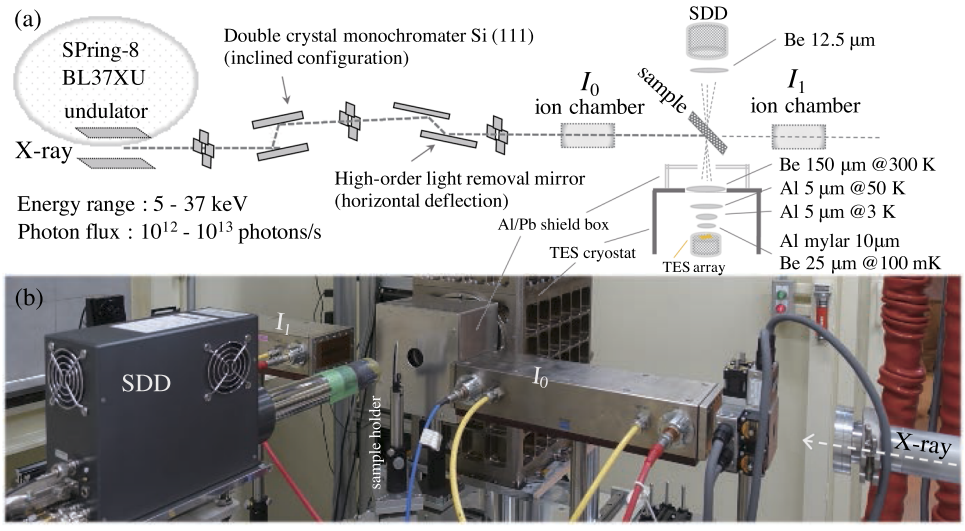


**FIG. 1**. (a) Overview of the experimental setup at BL37XU at SPring-8. The TES is set at the front side of the sample at an angle of 45°, while the SDD is on the opposite side. (b) The picture of the setup. The TES cryostat is covered with an aluminum box with a lead shield inside to prevent stray light from reaching the detector.

of intensities of an incident x ray ($I_0$) and a transmitted x ray ($I_1$).

Each TES consists of a superconducting bilayer of thin Mo and Cu films. An x-ray absorber of 4 $\mu$m thick Bi is deposited on top of the TES. Each pixel has an active area of 320 × 305 $\mu$m$^2$, which is determined by a gold-coated 275 $\mu$-thick Si aperture chip placed on top of the TES array, which prevents x rays from hitting the array outside of the x-ray absorbers; otherwise, x-ray heating of the substrate could deteriorate the energy resolution. The holes of the aperture chip are patterned by dry etching to have the same shape as the TES absorbers, so it does not obscure the x rays passing from the holes to the TES array. The total active area of the 240-pixel array is about 23.42 mm$^2$.

The detectors are cooled through a combination of a pulse tube cooler (Cryomech PT407 with a remote motor) and an adiabatic demagnetization refrigerator (ADR). Cooling from room temperature takes 17 h, plus an additional 1 h to cycle the ADR. This results in a TES bath temperature of 75 mK ± 4 $\mu$Krms. The ADR also provides an additional cold stage at 500 mK, where some of the readout electronics are mounted. The TES pixels are then electrically biased to their superconducting critical temperature of $T_C \sim 100$ mK.

Since the normal resistance of the TES is on the order of ~10 mΩ and its change caused by the x ray is on the order of ~mΩ, the signal needs to be read out by a low-impedance amplifier, such as a superconducting quantum interference device (SQUID). The voltage fed back to the feedback coil coupled to the SQUID is proportional to the time derivative of the resistance initiated by the absorption of an x ray. Details of the room temperature electronics are summarized in Ref. 21. The TES array uses a time-division-multiplexing readout system, which samples the current signal of the 240 sensors by dividing them into 8 SQUID columns. The sampling time of each sensor is 7.2 $\mu$s (=240 ns × 30 pixels), and thus, the effective sampling rate is 139 kHz. A record of 1024 samples (=7.3728 ms) was captured for each x-ray event. This length is changeable to any value in the software so that it can be chosen to match the length of the x-ray pulses. Unlike with an SDD, obtaining optimal energy resolution from a TES requires the application of a matched filter (optimal filter)[22,23] to the detector signal. Currently, the room-temperature hardware writes the entirety of these records for every trigger event to a storage disk at high speed, and the off-line software is used to do post-processing of pulse-shape analysis to achieve the best possible energy resolution. This implementation of saving the x-ray pulses causes the data quantity produced by the TES to be larger by three orders of magnitude than that of a SDD.

The x-ray absorber and TES are cooled at the coldest stage of the ADR. There are four windows between room temperature and the cold stage that are intended to reduce IR/vis/UV light on the TESs while transmitting most x rays: a 10 $\mu$m aluminized mylar and 25 $\mu$m Be at 50 mK, 5 $\mu$m Al at 3 K, 5 $\mu$m Al at 50 K, and a 150 $\mu$m Be window at the vacuum shield at room temperature. The detection efficiency is shown in Fig. 2. The 50 mK shell is made of the Al superconducting magnetic shield except for the x-ray window, although Al in the aluminized mylar might work to some extent. The distance of the TES to the sample is 15 cm. In this setup, the air outside the evacuated cryostat absorbs x rays more than the filters. The quantum efficiency of 4 $\mu$m-thick Bi is ~80% at 6 keV and ~20% at 13 keV, while it increases to ~40% above the L-edges of Bi. There are two limiting factors on the largest detectable energy: the

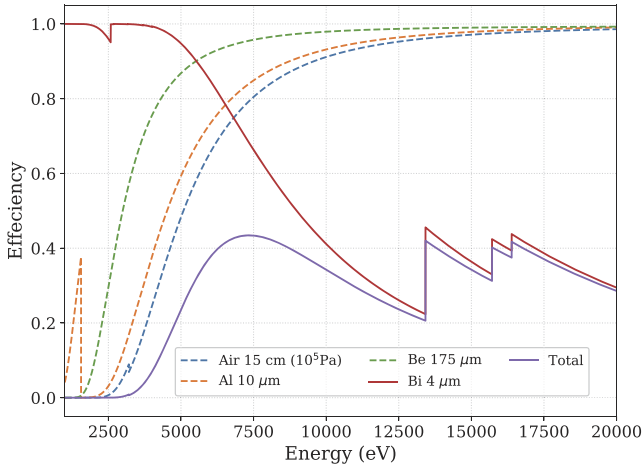


**FIG. 2**. The theoretical quantum efficiency of the TES is shown. The transmission of air (15 cm, $10^5$ Pa), Al filters (5 $\mu$m at 3 K and 5 $\mu$m at 60 K), Be windows (150 $\mu$m at 300 K and 25 $\mu$m at 100 mK), the photo-absorption efficiency of the 4 $\mu$m-thick Bi absorber, and the total efficiency are shown in blue dotted, yellow dotted, green dotted, red solid, and purple solid lines, respectively.

temperature of TES increases above $T_C$ due to the huge thermal input from x rays and the input signal to SQUID exceeds its linear range. The limit also depends on the bias voltage applied to the TES. We set the bias voltages to keep ~20% of the normal resistance of TES at $T_C$. Using the setup, photons below about 18 keV can be measured with the system.

The TES, which is a thin film in an intermediate phase between the normal and superconducting state, is sensitive to small magnetic fields, so a few percent of the Earth's magnetic field could deteriorate the sharp edge of the transition. There are two magnetic shields made of a high permeability metal at the 50 K and 3 K shells and a shield made out of a type I superconductor at 50 mK. The shielding effect is locally weak at the apertures for x rays since they are made of thin filters. Therefore, if there is a leak of a magnetic field along the incoming x-ray path, it could worsen the performance of the detector. However, at the BL37XU at SPring-8, the detector worked without any empirical sign of magnetic interference through the apertures.

### B. Energy resolution

The limit of the energy resolution of a TES is proportional to the temperature of the detector and the square root of heat capacity, while the total energy range is positively correlated with the heat capacity. The thickness and size of the x-ray absorber is designed to meet the scientific requirement for a particular experiment. The TES used in this experiment was optimized for the detection of 6 keV x rays. In an actual measurement, the energy resolution does not reach the theoretically derived value. This is because, as is typical in other low-temperature detectors, electrical and magnetic interference or mechanical micro-vibration can increase additional noise terms. This is one of the technical challenges of the application of the TES. Reproducing the best detector performance when the spectrometer is moved from one place to another requires a detailed

design of the TES system and the method for integrating it into the facility.

In our case, based on the experiment led by the High-resolution Exotic Atom x-ray spectroscopy with Transition-Edge Sensor (HEATES) collaboration,[24] the electrical interface of the vacuum chamber and the detector system was designed to be electrically isolated from both the pulse tube's compressor and the equipment of the beamline when it was installed. When we confirmed the basic performance in our laboratory, the compressor was electrically isolated from the cryostat. However, in practice, this configuration may not be the best due to the different grounding conditions. In SPring-8, we found that the temperature fluctuation of the 75 mK stage was 4 $\mu$Krms when the TES was grounded to the ground of the beamline, whereas the fluctuations increased by an order of 2 when floated. The isolation transmitters, which transfer electric surges by magnetic coupling, and the power stabilizers, which are capable of suppressing high frequency and regulating voltage automatically, were inserted into the power lines of the TES system. During commissioning, this configuration gave temperature fluctuations of ~4 $\mu$Krms and no additional noise components in the detectors. Note that this configuration means that the compressor of the pulse tube, the SDD, and other electronics in the beamlines were connected to TES through a low impedance, and thus they could affect the performance of the TES if any of them are not properly grounded.

The energy resolution is evaluated using $^{55}$Fe isotopes in this configuration. Although the K$\alpha$1 and K$\alpha$2 of Mn can be modeled with two lines when it is in a neutral gaseous state, as a solid, the emission spectrum must be fitted with a model consisting of a sum of eight Voigt functions, which is empirically derived by using crystal spectrometers.[25] The TES is assumed to have a Gaussian response. However, the Bi absorber is known to have a low energy tail, so the tail effect is taken into consideration according to Tatsuno *et al.*[26] The low energy tail is caused by the trapping of some of the heat carriers along grain boundaries in the evaporated Bi absorber. Recently, this issue has shown to be solved by using bismuth electroplated onto a Au seed layer, which increases the bismuth grain size, which nearly eliminates the low energy tail.[27] The typical amount of the tail in our TESs is ~20% at 6 keV, and the exponential decay length is ~20 eV. The energy resolution of each pixel is measured by including Gaussian broadening and the low energy tail in the response function and presented as a physical pattern of the detector in Fig. 3. The energy resolution is expressed as full width at half maximum (FWHM) throughout this paper. Some of the pixels were not electrically connected or not biased due to physical or electrical problems. These energy resolutions are equivalent to the best values obtained by this instrument at the J-PARC hadron environment.

We measured the energy resolution as a function of energy using the beam. We used a film of Pb to elastically scatter different beam energies and obtained the energy resolution by fitting the line with a Gaussian profile. The result is shown in Fig. 4. The count rates were set at ~1 kc/s (all pixels) at energies above 6 keV; the maximum beam intensity available at 5 keV produced a count rate of only 220 c/s (all pixels) for the current setup. In contrast to Fig. 3, the outlier values in Fig. 4 could be caused by high count rates due to Bragg reflection in the materials, although this needs further investigation.

This degradation in energy resolution at higher energies is believed to be caused by non-linearity of the transition curve of the

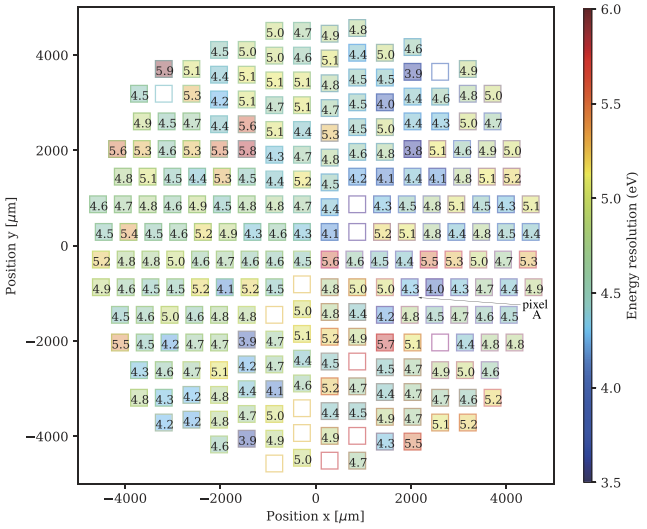


**FIG. 3**. The map of the energy resolution of the TES pixels. This map reflects the physical location of each pixel, with each sensor's energy resolution is shown on its position. The color bar linearly scales with the energy resolution. The pixels that were not operated are not colored. The location of pixel A is indicated with the arrow.

TES and their readout system. One non-linear effect is that the resistance of the TES is non-linear as a function of temperature, which is more significant as it gets closer to the normal resistance. The change in resistance is read out and amplified by SQUIDs, which are

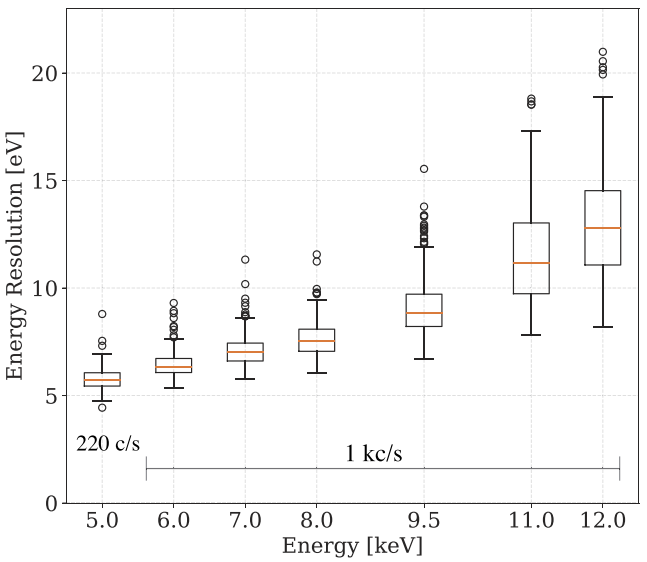


**FIG. 4**. The energy resolution at different energies obtained by elastic scattering from a Pb target. The box extends from the lower to upper quartile values of the energy resolutions in 220 pixels, with a horizontal line at the median. The upper whisker extends to the last datum less than $Q_3 + R \times 1.5$, while the lower whisker extends to the first datum greater than Q1 $- R \times 1.5$, where $Q_3$ and $Q_1$ are the upper and lower interquartile and $R = Q_3 - Q_1$. Beyond the whiskers, data are considered outliers and are plotted as individual points.

operated in the feedback mode called a flux-locked loop to linearize its output; however, the output voltage becomes slightly non-linear as the size of the input signal increases. These effects cause the pulse size to grow more slowly than the photon energy, which leads to a degradation in energy resolution. These non-linear effects also cause the pulse shape to change with the photon energy. Since the optimal filtering algorithm is based on the assumption that the signals are proportional to energies and the noise is stationary, the non-linear effects in a realistic environment could violate this assumption. This is why the energy resolution degrades at higher energies and has to be experimentally evaluated.

### C. Energy calibration

The relation between pulse height and energy is determined with Cr K$\alpha$, Co K$\alpha$, Cu K$\alpha$, Cu K$\beta$, Ge K$\alpha$, Ge K$\beta$, Br K$\alpha$, and Br K$\beta$. They are generated by fluorescing a pellet of $Cr_2O_3$, CoO, CuO, $GeO_2$, and KBr using a supporting agent of boron nitride with a beam energy of 14 keV. The example of an energy scale from pixel A is shown in Fig. 5. The data points are fitted with a third-order B-spline in log–log space, which does not pass through the origin. The nonlinearity of the TES response becomes more pronounced at higher energies due to the TES's approach to its normal-state resistance at the top of higher-energy pulses. We created energy calibration curves for each pixel at every ADR recycle. The gain of the system drifts by ~0.01% over ~10 h. It is caused by the variation in the temperature of the second stage of the ADR from roughly 500 mK to 1 K over 24 h, which affects the gain via multiple independent mechanisms. The gain drift is strongly correlated with the pretrigger (256 samples before the trigger), and thus, most of the correlation between the pulse height and the pretrigger is removed by the "drift correction" step.[23] After this correction, the effect is reduced to a scale of about 1 eV over 10 h after the ADR recycle and can often be further reduced with a correction based on a slowly varying function of time. If we assume that this effect adds in quadrature with other sources of the energy resolution, then we might expect it to degrade a 10 h long co-added spectrum from a detector with a 5 eV resolution to one with a 5.1 eV resolution. More careful treatment is required for longer measurements or when the absolute energies of emission lines is a goal of the measurement. In this application, a typical measurement duration is less than 2 h, so the effect of the gain drift is small. Additionally, the dependence of filtered pulse heights on the exact pulse-arrival time needs to be corrected,[23] although the arrival time contributes less than does gain drift to the energy resolution because the sampling rate is fast enough to track the rising profile of the pulse. After applying these corrections, converting pulse heights to energy via the best-fit calibration curve for each pixel and adding the histogrammed counts for all pixels, we obtain the final emitted x-ray spectrum. The inset in Fig. 5 shows the Cu K$\alpha$ line, which is well-fit to the Hölzer line shape[25] convolved with a Gaussian line shape and an exponential low-energy tail.

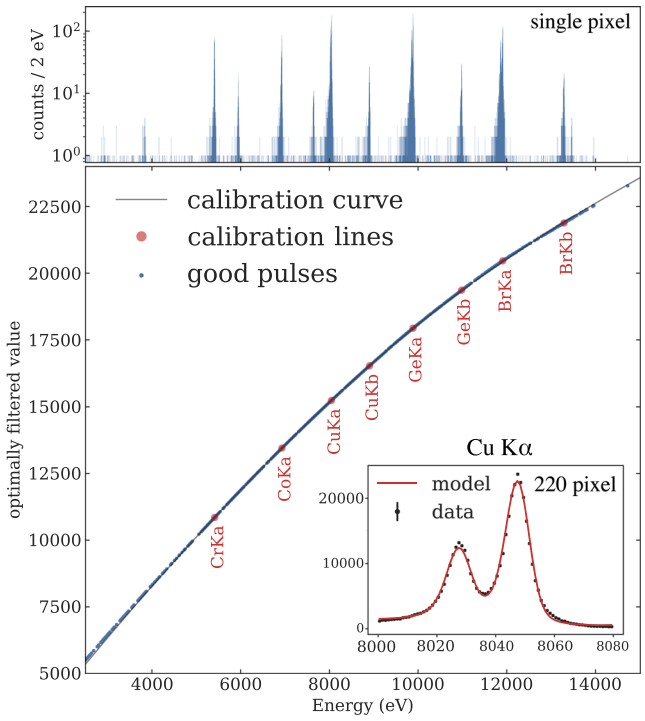


**FIG. 5**. Top panel: the energy spectrum of calibration sources taken from a single pixel A. Bottom panel: the obtained relation of pulse height and energy from pixel A. The red points are emission lines from Cr, Co, Cu, Ge, and Br, and the approximate calibration curve is overlaid. The inset shows, for the Cu K$\alpha$ line, the summed spectrum over 220 pixels (black points) and the fitted line profile (red solid line).

### D. High rate tolerance

The decay time constant of our TESs is about 1 ms. In order to qualitatively assess the degree of pileup, we define the pileup fraction: $f_{\rm pf}(x)$ is the ratio of $P(k \geq 2, x)$ to $P(k \geq 1, x)$, where $P(k, x)$ is the Poisson distribution function, $x$ is defined as the mean number of input x rays for a pixel per one record time $T_s$, and $k$ is the integer number of photons per $T_s$. The mean number of x rays per pixel per record time is related to the input x-ray rate per pixel, $r$, as $x = r \times T_s$. Then, the pileup fraction, $f_{\rm pf}(x)$, is expressed as

$$f_{\rm pf}(x) = \frac{\Sigma_{k=2}^{\infty} P(k,x)}{\Sigma_{k=1}^{\infty} P(k,x)} = \frac{1-(1+x)e^{-x}}{1-e^{-x}} = \frac{1}{2}x - \frac{1}{12}x^2 + O(x^4). \quad (1)$$

The pileup fraction is plotted as a function of $r$ in Fig. 6 with a nominal $T_s$ (=7.37 ms), as well as with an order of magnitude higher and lower values for comparison. When $r$ = 10 c/s pixel$^{-1}$ or 2200 c/s 220 pixels$^{-1}$, the pileup fraction is ~3%; while when $r$ = 100 c/s pixel$^{-1}$, the pileup fraction is larger than 30%. Thus, the input x-ray rate is adjusted in the range below $r$ ~ 10 c/s pixel$^{-1}$. When the pulse decay time constant is longer, such as in a gamma-ray TES, which might have a ten-times slower decay time than an x-ray TES, the limit would be lowered by an order of magnitude. In contrast, a faster TES is better unless the shorter readout time worsens the energy resolution.

In this experiment, we discard data records in which there is more than one x-ray arrival. However, in some applications of microcalorimeter arrays, the detection efficiency is a critical enough parameter that more effort is made to recover pileup events. One of

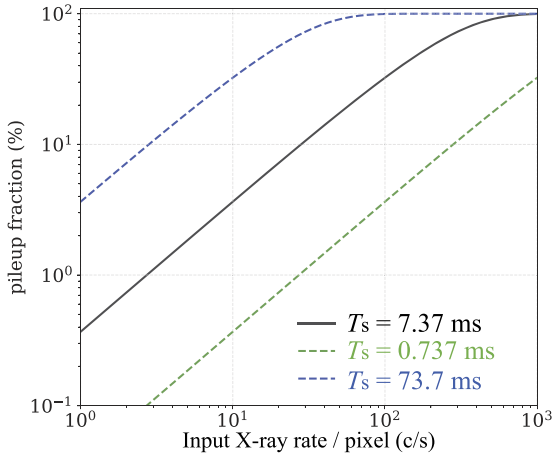


**FIG. 6**. The theoretical pileup fraction (%) vs incoming x-ray count rate per pixel. The pileup fraction for the nominal $T_s$ is shown as a black solid line. For reference, the pileup fractions for data-record lengths that are ten times shorter and longer than the nominal length are shown in green and blue dashed lines, respectively.

the advanced examples is implemented in the onboard pulse shape processor (PSP) in the ASTRO-H SXS. The program in a real-time OS can subtract a template waveform from the primary pulse and estimate the pulse shape of the subsequent event. Their system can detect two events that are separated by more than 2 ms, provided that the two adjacent pulses have a pulse amplitude contrast of a factor of 1/30 or more.[28] The ratio of the rise time of an x-ray event to the sampling time sets the calculation speed of this triggering algorithm. This ratio is similar in ASTRO-H (~4 ms to 80 $\mu$s) and our detector (~0.4 ms to 7.2 $\mu$s), so the ASTRO-H algorithm would work for our detector. Another method for the detection of nearly coincident events is described.[29] However, the energy resolution of the secondary events will deteriorate due to both the non-linearity of the pileup x-ray pulses and inaccuracy of the subtraction of the primary x-ray pulse. To put the secondary-event analysis into practical application, a significant effort such as that done for ASTRO-H SXS[30] is necessary. We discarded pileup records to simplify the analysis, but further studies on the pulse processing could improve our detector's throughput.

In this experiment, we evaluated the performance of the detector vs the input x-ray count rate. A film of $MnO_2$ was illuminated by a 6.6 keV beam, with seven different beam intensities that produced rates of triggered data records, summed over the 220-pixel TES array, between 400 c/s and 12 000 c/s. Figure 7 (top panel) plots the rate of triggered data records vs the flux of x rays incident on the sample. We sorted the data records into two categories: good and bad. Data records in the "good" category contain only a single x-ray arrival, while the "bad" data records include records that contain multiple piled-up x-ray arrivals, failed operation of the flux-locked SQUID for the readout of TES, and any other anomalously shaped pulses. The "total" record rate is the sum of the good and bad record rates. As the input count rate increases, the fraction of bad data records increases. The plot also shows the rate of good data records in an energy window around the Mn K$\alpha$ line.

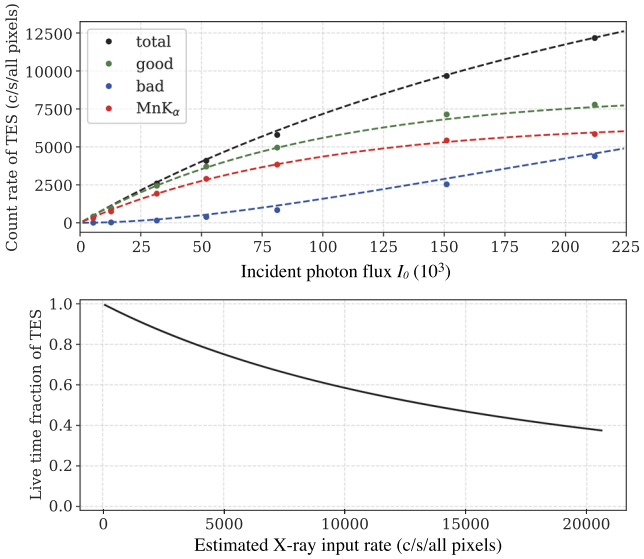


**FIG. 7**. Top panel: the array rate of data records of various types vs the flux of x rays on the sample measured with the ion chamber: the total, good, bad, and Mn K$\alpha$ record rates are shown in black, green, blue, and red, respectively. The $r'_{\text{total}}$, $r'_{\text{good}}$, $r'_{\text{bad}}$, and $r'_{\text{Mn}}$ are overlaid in a dashed line with the corresponding color. Bottom panel: the live time fraction, $f_{\text{live time}}$, is plotted as a function of an estimated x-ray input rate per TES, $r$.

The true input count rate of x rays per TES pixel is $r = pI_0$, where $I_0$ measures the beam flux incident on the sample via the current in an ion chamber and $p$ is a proportionality coefficient. Our spectrometer does not measure $r$ directly. Instead, we measure the rates of triggered data records, $r'$. The record rates of good, bad, and Mn K$\alpha$ are defined as $r'_{\text{good}}$, $r'_{\text{bad}}$, and $r'_{\text{Mn}}$. We phenomenologically estimated the detection efficiency by modeling the obtained data in Fig. 7 (top panel) using the following equations:

$$r'_{\text{total}} = \frac{1}{1 + T_s r} r \equiv Dr \quad (\text{c/s pixel}^{-1}), \tag{2}$$

$$r'_{\text{good}} = D^2 r \quad (\text{c/s pixel}^{-1}), \tag{3}$$

$$r'_{\text{bad}} = r'_{\text{total}} - r'_{\text{good}} \quad (\text{c/s pixel}^{-1}), \tag{4}$$

$$r'_{\text{Mn}} = k r'_{\text{good}} \quad (\text{c/s pixel}^{-1}), \tag{5}$$

where $r = 9.2 \times 10^{-2} I_0$ and $k = 0.78$, whose coefficients are obtained by comparing the data in Fig. 7 with the equations. They are overlaid in Fig. 7 (top panel). Figure 7 (bottom panel) shows the live-time fraction, $f_{\text{live time}} = r'_{\text{good}}/r$, or the fraction of input x rays that produce good data records vs the estimated x-ray input rate over the TES array. The dead time fraction, a fraction of time during which the TES pixel cannot write a data record that contains only one x-ray arrival, is written as $1 - f_{\text{live time}}$.

High count rates also affect the energy resolution. Figure 8 shows the energy resolution as a function of the TES trigger rate. The energy resolution is obtained by removing the bad events and

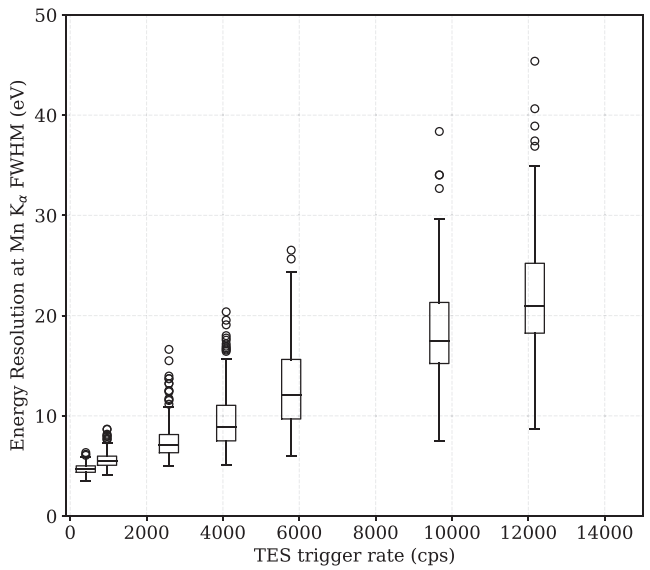


**FIG. 8**. Energy resolution at the energy of the Mn K$\alpha$ line against the TES trigger rates of all pixels (=the total count rate of all TES pixels). The notation of the plot is the same as in Fig. 4.

then fitting the spectrum of each pixel to the line shape of Mn K$\alpha$.[25] The energy resolution worsens with the increase in the count rate due to crosstalk among the TES pixels, which was not removed in this analysis. A shorter record length could improve the energy resolution at higher count rates, although an energy calibration would need to be carefully performed.[31]

## III. RESULTS

### A. Simultaneous multi-element analysis

To demonstrate the capabilities of the TES at BL37XU in SPring-8, a NIST standard reference glass (NIST SRM 610)[32] is used as a target. Figure 9 shows the spectra of SRM610 as measured by the TES and the SDD. The TES spectrum is a sum of 220 pixels accumulated for 10 min, while that of the SDD is from 0.5 min. The difference in the count rates is due to geometrical effects and the materials between the detector and the target. The spectrum of the SDD in Fig. 9 is composed of several sharp peaks. Since the energy of K lines is approximately proportional to the square of the atomic number, $Z$, the K$\alpha$ complexes in the energy range of 4 keV–13 keV occur every few hundred eV. The intensity ratios of the K$\alpha$ and K$\beta$ lines are about 10 to 1, although their rates are weakly dependent on the chemical composition. The L lines from high $Z$ elements complicate the line identification in the spectrum. As shown in the spectra in the inset of Fig. 9, the spectrum of the SDD around the Ni K lines appears to be a single peak, while the TES can resolve L lines from Yb, Ho, and Lu in addition to the Ni K lines.

To fit the spectrum with an estimated one (so-called model), the relevant physical processes including fluorescence emission, the photo-absorption, and the detector response are calculated to produce an expected spectrum. The free parameters to generate the expected spectrum are the Gaussian energy resolution of the TES, the exponential low-energy-tail fraction of the TES response, the constant level of the background, and the abundance of each element in the composition of the reference glass. The number of the free parameters is three plus the number of the elements. The line energies and the intensity ratios are fixed to the reference value obtained from *xraylib*.[33] This simplifies a parameterization of the model, reduces the computational time, and enables us to estimate the relative abundance.

The geometry is approximated by assuming that the sample is at 45° to both the beam and the TES. The x-ray intensity of fluorescence lines just outside the sample is calculated as follows: (1) The incident x-ray, $E_{\rm in}$ = 14 keV, is photo-absorbed along at the depth of $x$ from the surface of the sample. (2) An x-ray fluorescence photon is emitted at $x$. (3) The fluorescence x rays are subject to photo-absorption within the sample itself. (4) The remaining photons can escape from the sample to the air. We define $\sigma^{\rm att}(E)$ as the photo-absorption cross sections for x rays with an energy of $E$, $\sigma_{\rm i}^{\alpha}(E)$ is the x-ray fluorescence cross section for a given atomic number $I$ and an excited state of $\alpha$, and $\rho \equiv \sum_i \rho_i$ is the sum of the number density over the element $i$. The intensity of the fluorescence line from an element

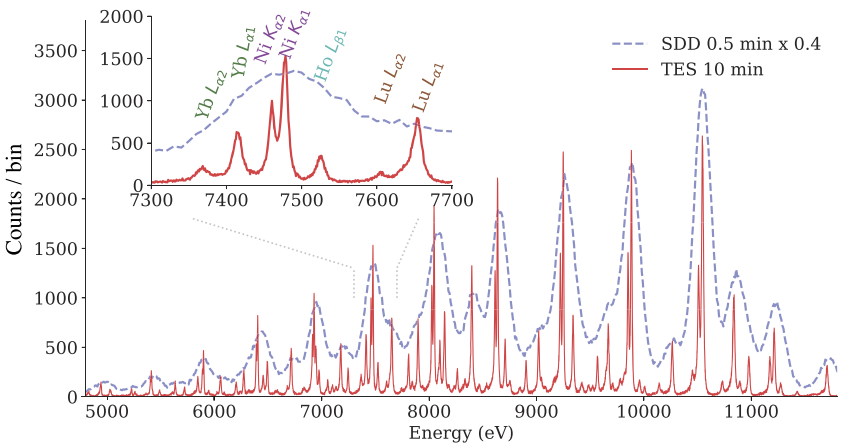


**FIG. 9**. The wideband spectra of SRM610 taken with TES and SDD. The bin sizes for the TES data and the SDD data are 1 eV and 10 eV, respectively. The energy of the x rays illuminating the target was 14 keV. The TES spectrum was created by summing over all pixels and integrating for ten minutes (solid red). The SDD spectrum was created from half a minute's data and overlaid in the plot by multiplying by a factor of 0.4 for visual clarity (dashed blue). The inset shows an example of the detailed comparison, where the TES can probe Yb, Ho, and Lu, which the SDD could not resolve due to the presence of strong Ni K lines.

$i$ and an excited state $\alpha$ is a function of the energy of the input beam $E_{\text{in}}$ and the energy of fluorescent x ray $E_\alpha$, which is expressed as

$$I_i^\alpha(E_{\text{in}}, E_\alpha) \sim \int_0^d \{N_0 e^{-\sigma^{\text{att}}(E_{\text{in}})\rho x}\}\{\sigma_i^\alpha(E_{\text{in}})\rho_i\} \times \{e^{-\sigma^{\text{att}}(E_\alpha)\rho x}\}dx, \quad (6)$$

where $N_0$ is the number of incident x-ray photons and $d$ is the depth of the sample. $\Omega/4\pi$, the solid angle of the detector from the sample, is included if the absolute value of the count rate is needed. The first factor of the integrand corresponds to the number of 14 keV x-ray photons, which reach a depth of $x$ from the sample surface. The second factor represents the amount of x-ray fluorescence induced by the 14 keV x-ray within the depth of $x \sim x + dx$. The escape probability of fluorescence x-ray photons is calculated using the third factor.

By performing the integral, Eq. (6) reduces to

$$N_0 \frac{\sigma_i^\alpha(E_{\text{in}})\rho_i}{(\sigma^{\text{att}}(E_{\text{in}}) + \sigma^{\text{att}}(E_\alpha))\rho}[1 - e^{-(\sigma^{\text{att}}(E_{\text{in}})+\sigma^{\text{att}}(E_\alpha))\rho d}]. \quad (7)$$

This represents the relative intensity of each transition. Since the thickness of SRM610 is about 1 mm and its density is 2.65 g/cm$^3$ according to Ref. 34, the exponential term can be ignored because it becomes almost zero, e.g., when the total (i.e., photoionization and Rayleigh and Compton scattering) attenuation cross section of iron $\sigma_{Fe}(E)$ (cm$^2$/g) as a function of an energy $E$ is considered for explanation, the exponential terms become $e^{-\sigma_{\text{Fe}}(6\text{keV})\times 0.1(\text{g/cm}^2)} \sim 0.0002$ and $e^{-\sigma_{\text{Fe}}(14\text{keV})\times 0.1(\text{g/cm}^2)} \sim 0.001$. The intensities of all the transitions are calculated and summed up to obtain the resulting model spectrum. Here, the model spectrum means that the spectrum of x rays escapes from the SRM610 target. The abundance of the elements, not the amplitudes of the individual lines, is floated in the fit. The transmission of the Al and Be filters, air, and the photoabsorption efficiency of the Bi absorber are taken into account, as shown in Fig. 2. Note that the scattered photons in the air are not negligible in the background spectra.

We fit the spectrum with the sum of the lines of known elements. The fit is done by comparing the model to the obtained spectrum and looking for the minimum of the residuals by changing the model parameters. The best-fit model and the residuals between the data and the model are shown in Fig. 10. There still remain some residuals between the spectrum and the model, which are probably due to uncertainties in the detector response and the line shape of some of the emission lines. Since the relative statistical errors in the spectrum are smallest near the peaks and are larger in the tails, the fitting to minimize the residuals divided by the statistical errors tends to converge to obtain the line intensities.

The resultant abundance ratio as a reference to Fe obtained from the best-fit model in Fig. 10 is shown in Fig. 11. The large number of photons creates small statistical errors, so the uncertainties of the fit are dominated by a systematic error. To obtain a rough estimation of systematic uncertainties, several representative lines are individually fitted in a narrow energy range around each line center. The results of the local fits are plotted in Fig. 11. The difference of the results between the global fit and the local fits gives a rough reference on the level of uncertainties. The reference value and its uncertainty of SRM610 are also plotted in Fig. 11. The fitting results are more or less consistent with those in the reference. The merit of the TES is to measure both light and heavy elements simultaneously in the hard x-ray band. Furthermore, resolving the lines can reduce the risk of misinterpreting the lines, and hence, the accuracy of the measurement is improved.

## B. XANES of heavy elements—As and Pb

Mapping a local area at the $\mu$m scale using XRF with a focused micro-x-ray beam is an important method to determine the distribution of trace and toxic elements in the ground, plants, and other

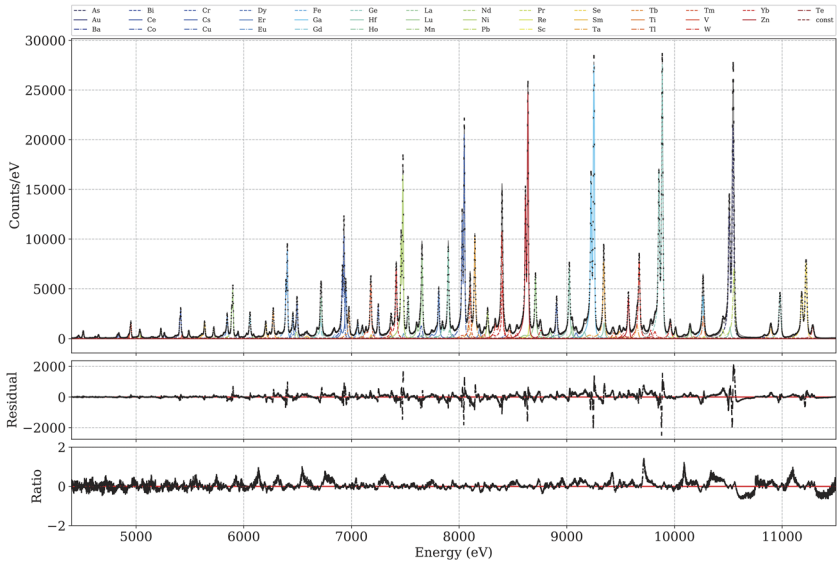


**FIG. 10**. Top panel: the example of simultaneous multicomponent fits for the XES of TES. The XES of TES and the best-fit model components are shown. Each element is plotted in different colors and line styles. Middle panel: the residual between the data and the model. Bottom panel: the ratio of the residuals, which is (data − model)/model.

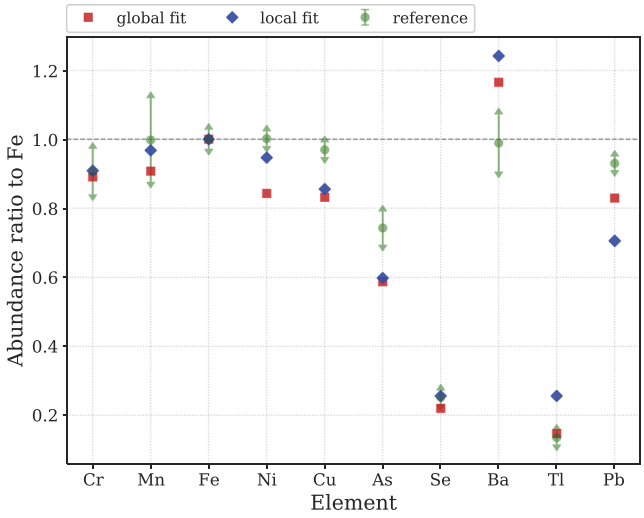


**FIG. 11**. The abundance ratios to Fe obtained by fitting the TES spectrum including the quantum efficiencies in Fig. 2 and the self-absorption in Eq. (3) are shown in red (global fit) and blue (local fit), respectively. The reference values are shown in green, where the uncertainties in the reference are plotted with arrows.

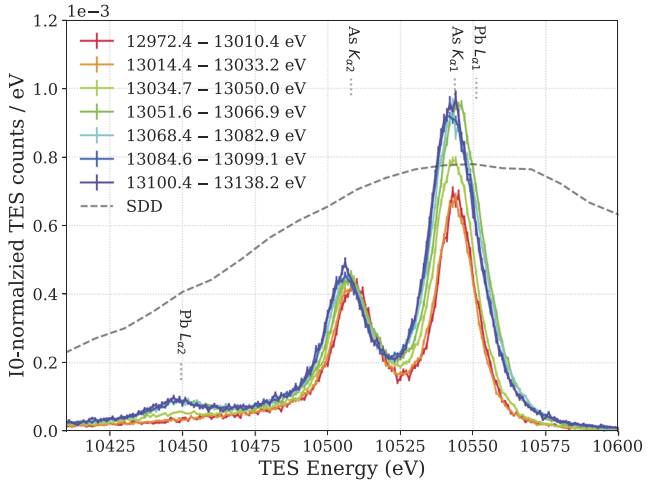


**FIG. 12**. X-ray emission spectra of the TES spectrometer with seven different x-ray energies illuminating a sample of SRM610 across the Pb $L_3$-edge (13 035 eV). The XESs are the seven snapshots of continuous data taken with TES when the bean energy sweeps from 12 970.3 eV to 13 138.2 eV. The energy scale of TES slightly varies from scan to scan due to calibration uncertainties and remaining gain drift even after a routine drift correction. When the input x-ray energy is below the Pb $L_3$-edge, only As K$\alpha$1 and K$\alpha$2 are present. As the energy increases, Pb L$\alpha$1 and L$\alpha$2 become prominent. As a reference, the spectrum as measured by an SDD when the input x-ray energy is above the Pb $L_3$-edge is overlaid with a dashed line.

forms of life, since the method can be directly applied to these samples under ambient conditions. In particular, coupling XRF with x-ray absorption fine structure (XAFS) spectroscopy has made it a powerful tool, since we can obtain species of the elements, which is the essential information to understand the environmental behavior of toxic elements. Among the various toxic elements, arsenic (As) and lead (Pb) are the most important elements in terms of their health risks and wide occurrence in the earth's crust (e.g., Ref. 35). These two elements frequently co-exist in specific environments such as in sulfide mine tailings and coal (e.g., Ref. 36), which warrants studying the environmental chemistry of the two elements in the same systems (see the works of Brown *et al.*[37] and Liu and Luo[38]). Lead has also been important in terms of its atmospheric pollution and as a potential risk to health.[39] However, determination and speciation of the two elements in the same sample can sometimes be challenging when using XRF and XAFS due to the difficulty in the separation of As K$\alpha$ and Pb L$\alpha$ emissions, since the energy resolution of an SDD is not sufficient to resolve the lines.

To overcome the difficulty of using an BCLA, XRF, and XAFS, using a TES is an important option. We scanned SRM610 across the Pb $L_3$ edge to demonstrate how the TES can contribute to the chemical diagnostics of heavy elements in complicated compounds. Figure 12 shows the seven snapshots of the TES spectrum of As and Pb when the beam energy sweeps from 12 970.3 eV to 13 138.2 eV. The sweep time is 60 s over the Pb $L_3$-edge energy, with 30 s in the pre/post-edge region. There are four emission lines in this band: 10 508.0 eV, 10 543.7 eV, 10 449.5 eV, and 10 551.1 eV corresponding to As K$\alpha$2, K$\alpha$1, Pb L$\alpha$2, and L$\alpha$1.

When using an SDD, the Pb L$\alpha$ and As K$\alpha$ lines may severely interfere with each other, which sometimes prevents Pb mapping using L$\alpha$ in the presence of abundant As (e.g., see Liu and Luo[38]). In this case, Pb L$\beta$ can be used for the speciation of Pb by sweeping x rays around the Pb $L_2$-edge. However, the Pb $L_2$-edge energy (15 200 eV) is identical to that of Rb K-edge (15 200 eV), both of which are commonly found in relatively high concentration (average concentrations in the upper continental crust of Rb and Pb are 112 mg/kg and 20 mg/kg, respectively; see the work of Taylor and McLennan[40]), which can cause another interference. Hence, it is prudent to focus on Pb L$\alpha$2, which is ~50 eV away from As K lines, to map Pb by XRF. Figure 13 shows XANES of the Pb $L_3$-edge (13 035 eV) measured by the TES. The statistical errors are calculated from the Poisson error of the number of counts in one step in the incident beam energy. The counts are divided by $I_0$ during each step and subtracted from the mean before the pre-edge region, and the XAFS spectrum is normalized at the post-edge region, the so-called "flat" region. The same is applied to other XAFS spectra. The detection limit of Pb L$\alpha$2 depends on the statistical uncertainty rather than systematic uncertainties on the contamination of neighboring lines. The selective detection of Pb L$\alpha$2 is difficult using an SDD due to its low energy resolution. As shown in Fig. 12, the XRF spectrum measured by SDD is a smeared sum of four peaks of As K$\alpha$1, As K$\alpha$2, Pb L$\alpha$2, and Pb L$\alpha$1.

Pb $L_3$-edge XANES is sensitive to the valence state of Pb, either Pb(II) or Pb(IV), and its coordination environment. The XANES of PbO, $PbSO_4$, and $PbO_2$ are overlaid as references in Fig. 13. The presence of any peaks or shoulders in the pre-edge region (small shelf in the blue line at 13 040 eV in Fig. 13) is indicative of Pb(IV) due to the electron transition from 2*p* to 6*s*, since the 6*s* orbital is empty for Pb(IV). The absence of such characteristics in the spectrum in Fig. 13 suggests that the 6*s* orbital is filled in this sample. Thus, the Pb in the sample is likely to have its origin in Pb(II).

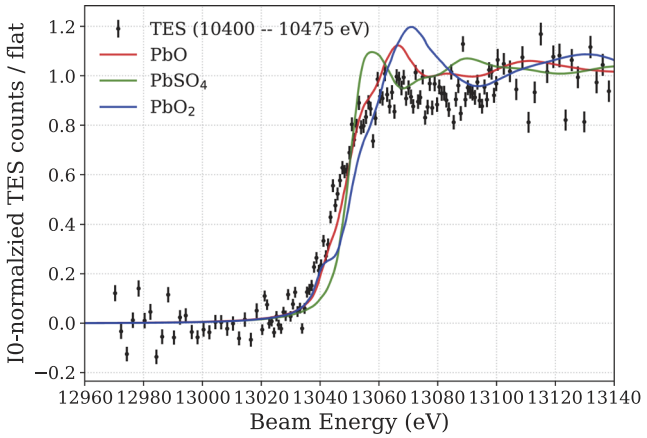


**FIG. 13**. The XANES of Pb Lα2. The counts in 10 400 eV–10 475 eV of TES are divided by $I_0$ counts, the mean below the pre-edge is subtracted, and the result is normalized at the post-edge (flat) region. The error bars refer to the statistical errors. The XANES taken from reference samples of PbO, $PbSO_4$, and $PbO_2$, are overlaid in red, blue, and green, respectively.

The use of TES enables us to measure Pb $L_3$-edge XAFS by detecting Pb Lα2 when the statistical errors from the tails of As Kα lines and the background are smaller than the signal from Pb Lα2. Note that the speciation of As using its K-edge XAFS does not interfere with Pb, since the absorption edges of Pb are higher than As K-edge. However, there is a huge demand for the speciation of Pb in the presence of As. Thus, fluorescence XAFS using a TES is worth considering as an option for a next-generation synchrotron facility.

### C. XANES of a dilute sample—Fe

Another application of the TES is to measure samples where the material of interest is very dilute. The high resolution can help resolve the signature of the elements of interest from the background and mitigate the risk of misinterpreting the spectra. Here, we chose a sample containing Fe (iron) in aerosol collected above the sea as a target for demonstration.

Iron is abundant in the Earth since it is the most stable nucleus of all the elements. It also plays an important role in controlling the Earth's environment. For example, the amount of Fe at the surface of the ocean affects the number of phytoplankton, which is related to the uptake of $CO_2$, and thus has implications for global climate change.[41,42] One of the important sources of Fe at the ocean surface is aerosols containing various species of Fe that originate from natural and anthropogenic sources.[43,44] The Fe species is important since highly soluble Fe species are preferentially dissolved in seawater and utilized by phytoplankton.[45,46] Although XAFS is an effective method to measure the speciation of iron,[47,48] precise measurement of marine aerosols is challenging since the amount of the aerosols above the sea is about three orders of magnitude lower than that collected on land.

The aerosol specimen was prepared in the same way as described in Ref. 49. The aerosol sample was collected during the *R/V* Hakuho-maru KH-17-3 cruise in the subarctic North Pacific. The aerosols were separated into six size-fractions, and one of them (size fraction: 0.49 μm–0.95 μm) was used for the analysis. Since the amount of the collected samples is very small, an acid-washed polytetrafluoroethylene (PTFE) sheet (Naflon tape, thickness = 0.2 mm, Nichias Co., Ltd., Japan) was used to minimize contamination from the sampling filter. Details on the preparation methods of the PTFE filter are described in Ref. 50. The amount of Fe of the sample was several ng of Fe per 1 $cm^2$ filter, which is measured by inductively coupled plasma-mass spectrometry (ICP-MS, Agilent 7700) after acid digestion of the aerosol sample based on our previous work.[50] Since we could not eliminate the contamination from Fe in the filter or the beamline, we took data from the aerosol sample on the PTFE filter and from a PTFE filter without an aerosol sample (a blank target).

The input energy ranges were 7086.9 eV–7180.4 eV for the aerosol and 7087.2 eV–7165.2 eV for the blank target to sweep from the pre-edge energy of Fe–K to the post-edge energy. The TES count rate was adjusted to be around 2 kc/s (array) by adjusting the slit when the beam energy is set at the post-edge region. Figure 14 shows the XES of the aerosol sample and the blank target, which are created by using all the time during the sweep just to clarify the difference in the spectra. The two XESs are normalized by integrating

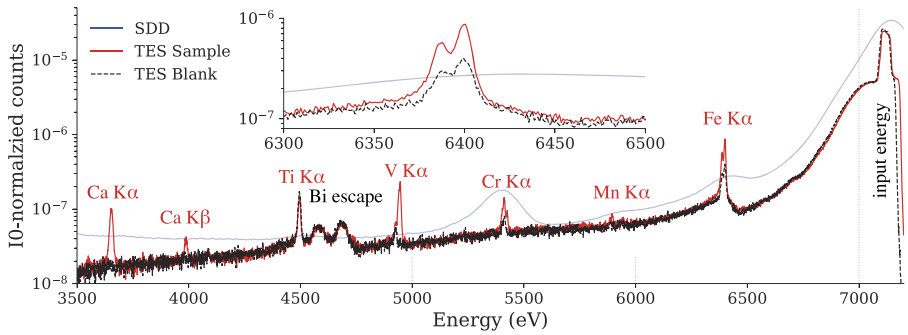


**FIG. 14**. The XES of TES taken from the aerosol sample (red) and the blank target (black). The data are accumulated during the period of the input x-ray sweeping from 7086.9 eV to 7180.4 eV for the aerosol and 7087.2 eV–7165.2 eV for the blank target, respectively. For comparison, the XES of SDD taken from the same sample is plotted in blue when the beam energy is fixed at 7131.58 eV. The vertical axis of TES is the counts per 1 eV bin divided by the $I_0$ intensity, while that of SDD is multiplied by an arbitrary factor for clarity. The inset shows a magnified view at the Fe Kα lines.

the counts/$I_0$, where both are a function of the beam energy. The excess of the weak lines from Ca, V, Cr, Mn, and Fe come from the sample. The width of the beam energy sweep is 93.3 eV (=7180.4 eV–7086.9 eV) for the aerosol, and the Bi escape peaks seen at 4600 eV–4700 eV are broad due to the sweep of the input energy. The same feature is seen in the XES of the blank target. For reference, the XES of SDD taken at a beam energy of 7131.58 eV is shown in Fig. 14. The interference of scattered x rays at the Fe region is more severe in SDD.

Figure 15 shows the XES of the two targets as the beam energy was swept across the Fe K-edge energy. The entire range of the scan is divided into ten segments and shown in different colors in Fig. 15. For reference, the count rate of the TES in the 6330 eV–6430 eV range for the aerosol specimen was 455c/60 s when the beam energy was 7086.9 keV and 1327c/60 s when the beam energy was 7180.4 eV. For the blank target, count rates were 183c/30 s at 7087.2 keV beam energy and 308c/30 s at 7165.2 eV, and $I_0$ did not significantly change during the sweep, which means that the counts from background Fe K lines were 25c/30 s (=308c/30 s–183c/30 s). The difference in the integration time (60 s for the sample and 30 s for the blank) is due to a schedule constraint. The energy resolution of the spectra in Fig. 15 is estimated from a valley between Fe K$\alpha$1 and Fe K$\alpha$2. A similar approach is used with manganese (see Fig. 7 [51]). This is a practical way of estimating the energy resolution because calibration uncertainties and cross talk and operational environments of the TES could cause failure of the fitting due to unexpected tails around the peaks. For the current measurement, a typical statistical error in each spectral bin is larger than a few percent, which means that it is difficult to assess chemical shifts of a peak energy, typically below 1 eV.[52] Also, another desirable analysis is to obtain the information on resonant inelastic x-ray scattering (RIXS),[53] although the statistical errors due to the high background and a limited number of photons hinder further analysis. A larger

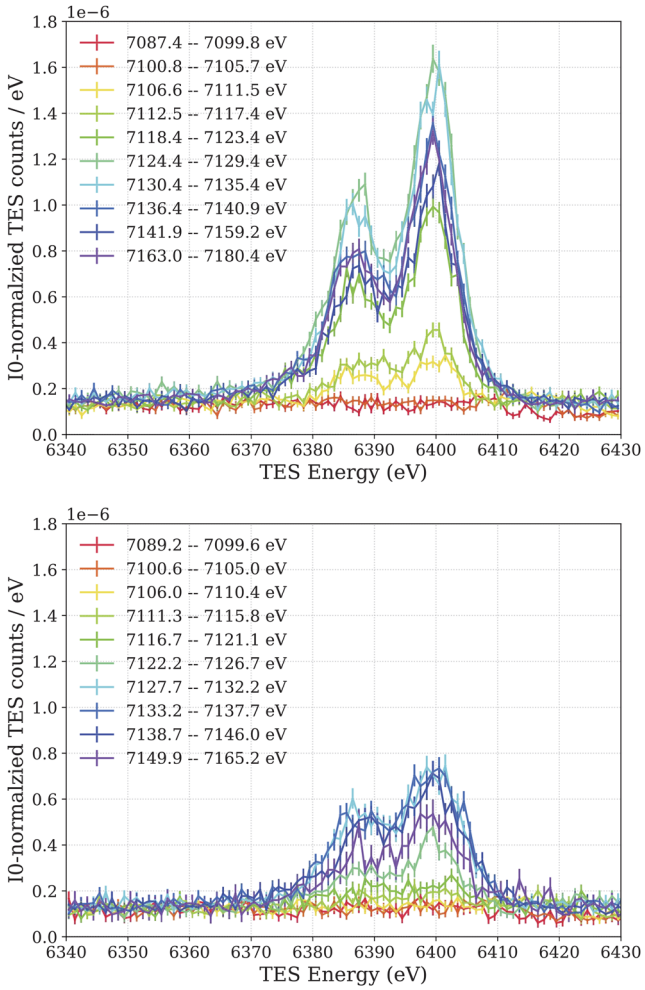


**FIG. 15**. Top panel: the Fe K$\alpha$1 and K$\alpha$2 spectra of the aerosol specimen for ten different beam energies, which are specified in the legend by different colors. The error bars refer to the statistical errors on the number of photons per energy bin. Bottom panel: the same measurement as above repeated for the blank target.

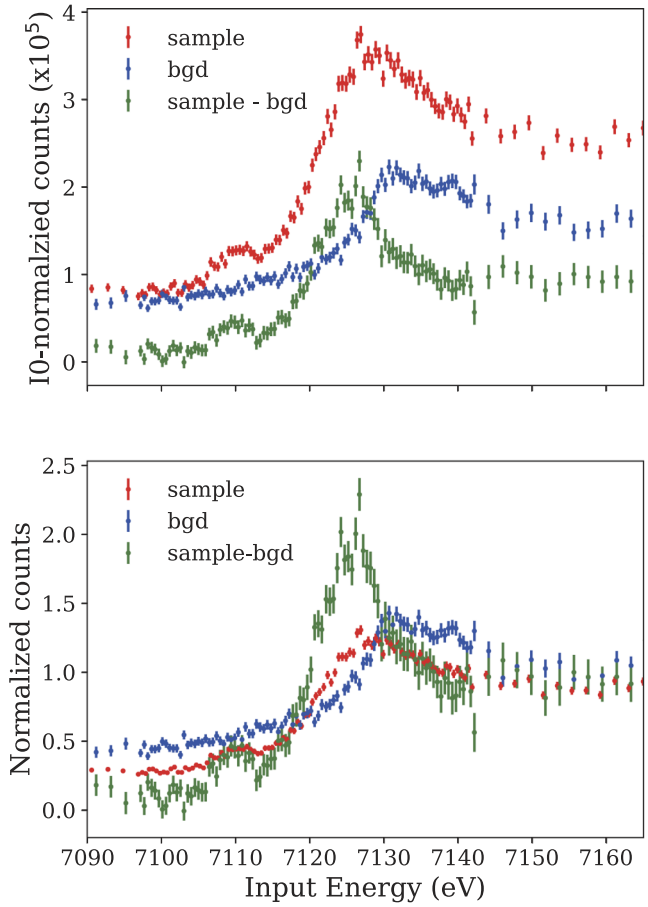


**FIG. 16**. Top panel: XANES spectra of the aerosol sample, the blank target, and the difference of the two are shown in red, blue, and green, respectively. The horizontal axis is the x-ray energy of the beam, while the vertical axis is the TES counts in the 6360 eV–6420 eV range normalized by $I_0$. Bottom panel: the same as above with the spectra normalized to their mean values at the higher end of the energy range.

effective area with more pixels and lower background would enable further improvement in application.

The XANES spectra are created by plotting the sums of the counts in TES from 6360 eV to 6420 eV and normalizing by $I_0$. The difference of the dead time fraction during the scan is corrected by using the good and bad event fractions, which are almost constant at ~3% across the input energy. Figure 16 shows the XANES spectra of the aerosol specimen, the background, and the difference between the two. The subtraction is performed in the unit of counts per $I_0$. This is based on the assumption that the background is scaled by $I_0$, which is valid assuming that the spatial distributions of the scattered, absorbed, and transmitted photons do not change over the specimen. The assumption is only valid when the specimen is thinner than the total attenuation length. However, if the specimen is thicker than the total attenuation length, it could change the irradiation environment, and thus, the background estimation using the blank target would be more difficult. The aerosol sample is almost invisible to the unaided eye, so it is in the former case.

The XANES of TES is compared to several possible references in Fig. 17, including XANES data of hematite, ferrihydrite, fayalite, and biotite that we obtained by ourselves in the transmission mode at the PF BL-12C in KEK. Hematite measured at both KEK and SPring-8 is used for calibration between the two beam lines. The energy of a pre-edge peak, corresponding to 1 s to 3*d*/4*p* transition of hematite, is 7111.2 eV as indicated by a vertical line in Fig. 17. This is used as an energy calibration of the beam energy. Of the reference spectra, the TES spectrum seems closest to that of biotite. It is confirmed by conducting the least-square fitting of the XANES spectra, and the spectrum measured by TES is best fitted by that of biotite. Biotite is abundant in mineral dust aerosols with a low Fe solubility, which could be a reasonable scenario for the source of this sample. By reducing contamination of Fe from the filter or the beamline and by estimating the background as above, the TES can be a powerful tool to investigate dilute quantities of Fe species in aerosols.

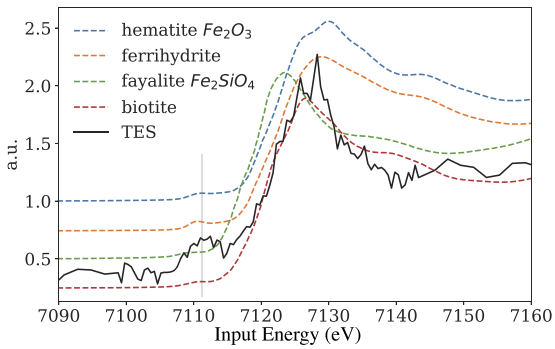


**FIG. 17**. Fe K-edge XANES spectra of reference compounds and the aerosol sample measured by the TES: hematite (blue), ferrihydrite (orange), fayalite (green), biotite (red), and the TES spectrum (black). The vertical axis is a normalized XANES spectra with constant offsets. The vertical line refers to 7111.2 eV, corresponding to 1*s* to 3*d*/4*p* transition of hematite.

## IV. SUMMARY AND DISCUSSION

The performance of a TES-based spectrometer for high energy resolution x-ray spectroscopy has been successfully demonstrated at the third generation synchrotron facility SPring-8. The TES spectrometer used was a NIST 240 pixel TES, which is a stable and technically mature instrument, and has therefore been deployed for many experiments worldwide. The utility of the TES for a particular XAFS application needs to be determined by considering the requirements for the energy resolution and the photon statistics in the region of interest. These parameters are not solely determined by the design of the TES spectrometer; the integration of the TES into the beamline and the sample under study also affect the count rates measured by the TES and consequently affects the energy resolution. The accuracy of the energy scale, which is necessary to measure the chemical shifts, depends on the availability of calibration lines in the scientific region of interest. Calibration lines must be produced with sufficient photon statistics for an accurate measurement, and effort in post-processing is required to meet specific calibration requirements. Therefore, successful application of a TES spectrometer at a synchrotron facility involves a series of collaborative and continuous efforts to optimize the performance of the detector and the accelerator to accomplish a particular scientific goal.

The performance of the TES spectrometer was studied over the energy range 4 keV–13 keV using a Mn target with varying count rates and a Pb target with varying beam energies. The energy resolution is ~5 eV FWHM at 6 keV at total count rates of <2 kc/s (array), which increases to a few tens of eV above 10 keV. Although there is still room for improvement in the energy resolution, we have demonstrated the ability of TES to simultaneously detect multiple elements in a standard sample. There are many lines that can be successfully separated by the TES, even with the current energy resolution. Figure 18(a) summarizes the number of emission lines

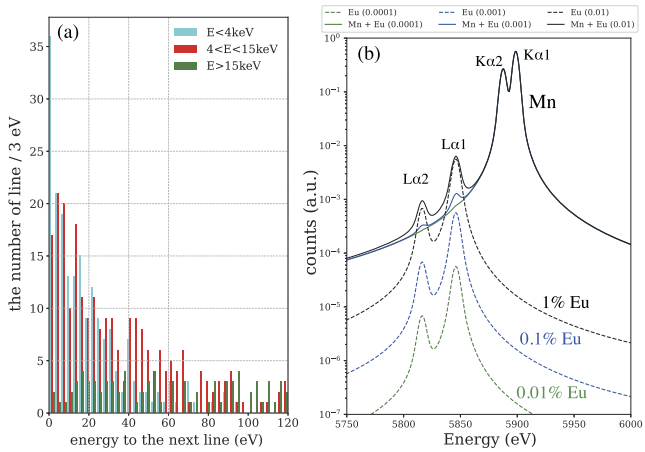


**FIG. 18**. (a) Distribution of the energy differences between one line and the next. The vertical scale is the number of fluorescence lines per 3 eV bin. The blue, red, and green ones refer to the samples in $E < 4$ keV, 15 keV $> E > 4$ keV, and $E > 15$ keV, respectively. (b) Simulated spectra of Mn and Eu using natural widths given an energy resolution of 5 eV. The efficiency shown in Fig. 2 is included, although it does not change the relative intensity within the narrow energy range. The mass fraction of Mn to Eu is 1:0.01 (black), 1:0.001 (blue), and 1:0.0001 (green).

as a function of the energy gap between lines using data from the X-ray Data Booklet compiled by Lawrence Berkeley National Laboratory.[54] Only the strongest lines for atomic numbers $3 \leqq Z \leqq 95$ are included: K$\alpha$1, K$\alpha$2, K$\beta$1, L$\alpha$1, L$\alpha$2, L$\beta$1, L$\beta$2, L$\gamma$1, and M$\alpha$1, which result in a total of 700 emission lines. The lines are divided into three energy ranges: <4 keV, 4 keV–15 keV, and >15 keV. The number of pairs of lines with an energy difference larger than 20 eV is 74 out of 198 pairs of lines in $E < 4$ keV, 155 out of 257 pairs in 4 keV $< E <$ 15 keV, and 228 out of 243 pairs in E > 15 keV, respectively. As an example of a realistic application, expected spectra of Mn and Eu are shown in Fig. 18(b). This assumes a study on rare earth elements in a natural sample. The efficiency shown in Fig. 2 is included in the calculation, and the lines with natural widths are convolved with an energy resolution of 5 eV without a tail component. The mass fraction of Eu has changed from 0.01%, 0.1%, and 1% of Mn. The detection of Eu could be possible when its mass fraction is larger than 0.1% of Mn, although it could be more difficult as it is smaller. Therefore, although there are many lines that can be distinguished by the energy resolution of the TES in the hard x-ray energy range, the requirements on experiments must be carefully assessed for each sample. One must consider the energy resolution, photon statistics, accuracy of the energy calibration, and the relative intensities of different atoms around the region of interest.

We have also demonstrated the measurement of XANES from Fe in a dilute environmental sample. In a practical application, Fe is one of the most difficult elements for the measurement because Fe is present in many of the support structures in both the beamline and the TES system. As shown in Fig. 14, the continuum of the background spectrum is almost the same as that of the sample. In this particular case, the difference between the spectrum of the sample and that of the blank target, which are normalized by $I_0$, can be identified as the excess of the weak lines from Ca, V, Cr, Mn, and Fe in the sample. Even if the value of $I_0$ is not accurately known, the normalization factor can be estimated by comparing the background continuum level. The method is only valid when the target is very thin in terms of the total attenuation length, e.g., $1/\sigma_{\mathrm{Fe}}(6\ \mathrm{keV}) \sim 0.012\ (\mathrm{g/cm^2})$ and $1/\sigma_{\mathrm{Fe}}(14\ \mathrm{keV}) \sim 0.014\ (\mathrm{g/cm^2})$. When the target is thick, it should change the shape of the background continuum and the relative intensities of the emission lines. In such a case, the absolute value of $I_0$ can be a unique reference for the comparison. However, setting the same level of $I_0$ for both the sample and the blank is operationally difficult. If the input x-ray rate at the absorber of the TES when a beam energy is in the pre-edge region is adjusted to be the same for both the sample measurement and the blank, the time for the measuring the blank could be longer than that when the beam intensity is optimized. In other words, once the setup is optimized without the sample, the input rate for the thick sample would be too large. Furthermore, if background lines originate somewhere along the beamline, such as in the pipes of the beamline that are made from alloys of Fe or chromium, the assumption that the background is scaled by $I_0$ may not hold. Although more systematic studies are needed to assess methods of background subtraction for thick samples, it is still the case that identifying the origin of the background components is aided by the high energy resolution of the TES, resulting in a better understanding of the environment of the experimental setup.

Development of TES technology is ongoing and will lead to performance improvements in terms of the number of pixels, the effective area, and the energy range of the sensor arrays. One of the breakthrough methods that has seen rapid progress in recent years is the readout of TES signals via microwave SQUID multiplexing,[55,56] which enables us to read about hundreds of pixels with only a few coaxial cables required to run from the cold readout stage to the room temperature electronics. Microwave multiplexing also provides a significant increase in the available readout bandwidth, enabling the readout of larger arrays and faster signals. Real-time processing capabilities are also under development, which are needed for the TES to be widely accepted by the x-ray science community. Future space applications or other remote instruments will require practical solutions, e.g., a space-flight compatible electronics[57] in terms of the detailed assessment on the digital electronics. When new technological developments enable more TES pixels and the energy resolution approaches the practical limit (~eV), the TES will find new applications in the study of the spatial and steric microstructure and for high-resolution XANES analyses such as RIXS[53] and the measurement of chemical effects.[58] Our results are useful as a benchmark of the performance of the current generation of TES spectrometers at a hard x-ray synchrotron facility.

## ACKNOWLEDGMENTS

This work was partly supported by the Grants-in-Aid for Scientific Research (KAKENHI) from the MEXT and JSPS (Grant Nos. 16H02190, 18H05458, 18H03714, 18H01260, 18H03713, 18H03892, 17H06455, 20K20527, and 19K21884) and the RIKEN Pioneering Project: Evolution of Matter in the Universe. The authors are grateful to the members of the NIST Quantum Sensors Project. We appreciate the significant contributions by SPring-8, J-PARC, RIKEN, and those who have backed up SPring-8 experiments (Grant Nos. 2019A1523, 2019B1498, and 2020A0174).

## DATA AVAILABILITY

The data that support the findings of this study are available from the corresponding author upon reasonable request.

## REFERENCES

[1]Y. Takahashi *et al.*, "Application of x-ray absorption near-edge structure (XANES) using bent crystal analyzer to speciation of trace Os in iron meteorites," Anal. Chim. Acta **558**, 332–336 (2006).

[2]D. Sokaras, T.-C. Weng, D. Nordlund, R. Alonso-Mori, P. Velikov, D. Wenger, A. Garachtchenko, M. George, V. Borzenets, B. Johnson, T. Rabedeau, and U. Bergmann, "A seven-crystal Johann-type hard x-ray spectrometer at the Stanford Synchrotron Radiation Lightsource," Rev. Sci. Instrum. **84**(5), 053102 (2013).

[3]S. Huotari, C. J. Sahle, C. Henriquet, A. Al-Zein, K. Martel, L. Simonelli, R. Verbeni, H. Gonzalez, M.-C. Lagier, C. Ponchut, M. Moretti Sala, M. Krisch, and G. Monaco, "A large-solid-angle x-ray Raman scattering spectrometer at ID20 of the European Synchrotron Radiation Facility," J. Synchrotron Radiat. **24**(2), 521–530 (2017).

[4]T. Takahashi *et al.*, "The ASTRO-H x-ray astronomy satellite," Proc. SPIE **9144**, 640–663 (2014).

[5]Y. Takei, S. Yasuda, K. Ishimura, N. Iwata, A. Okamoto, Y. Sato, M. Ogawa, M. Sawada, T. Kawano, S. Obara, C. Natsukari, A. Wada, S. Yamada, R. Fujimoto, M. Kokubun, N. Y. Yamasaki, H. Sugita, K. Minesugi, Y. Nakamura, K. Mitsuda,

T. Takahashi, S. Yoshida, S. Tsunematsu, K. Kanao, K. Narasaki, K. Otsuka, F. S. Porter, C. A. Kilbourne, M. P. Chiao, M. E. Eckart, G. A. Sneiderman, J. T. Pontius, D. McCammon, P. S. Wilke, and J. Basile, "Vibration isolation system for cryocoolers of soft x-ray spectrometer on-board ASTRO-H (Hitomi)," J. Astron. Telesc. Instrum. Syst. **4**, 011216 (2018).

[6]Hitomi Collaboration, Nature **535**, 117–121 (2016).

[7]K. D. Irwin and G. C. Hilton, *Transition-Edge Sensors* (Springer Berlin Heidelberg, Berlin, Heidelberg, 2005), pp. 63–150.

[8]K. D. Irwin, G. C. Hilton, D. A. Wollman, and J. M. Martinis, "X-ray detection using a superconducting transition-edge sensor microcalorimeter with electrothermal feedback," Appl. Phys. Lett. **69**(13), 1945–1947 (1996).

[9]W. B. Doriese *et al.*, Rev. Sci. Instrum. **88**, 053108 (2017).

[10]X. Barcons *et al.*, J. Phys.: Conf. Ser. **610**, 012008 (2015).

[11]S. Okada *et al.*, Prog. Theor. Exp. Phys. **2016**, 091D01.

[12]T. Hashimoto, M. Bazzi, D. A. Bennett, C. Berucci, D. Bosnar, C. Curceanu, W. B. Doriese, J. W. Fowler, H. Fujioka, C. Guaraldo, F. Parnefjord Gustafsson, R. Hayakawa, R. S. Hayano, J. P. Hays-Wehle, G. C. Hilton, T. Hiraiwa, Y. Ichinohe, M. Iio, M. Iliescu, S. Ishimoto, Y. Ishisaki, K. Itahashi, M. Iwasaki, Y. Ma, H. Noda, H. Noumi, G. C. O'Neil, H. Ohnishi, S. Okada, H. Outa, K. Piscicchia, C. D. Reintsema, Y. Sada, F. Sakuma, M. Sato, D. R. Schmidt, A. Scordo, M. Sekimoto, H. Shi, D. Sirghi, F. Sirghi, K. Suzuki, D. S. Swetz, K. Tanida, H. Tatsuno, M. Tokuda, J. Uhlig, J. N. Ullom, S. Yamada, T. Yamazaki, and J. Zmeskal, "Beamline test of a transition-edge-sensor spectrometer in preparation for kaonic-atom measurements," IEEE Trans. Appl. Supercond. **27**(4), 2100905 (2017).

[13]R. Maisonobe and the EDELWEISS Collaboration, J. Low Temp. Phys. **193**, 1129 (2018).

[14]A. Nucciotti *et al.*, J. Low Temp. Phys. **193**, 1137 (2018).

[15]S.-J. Lee, C. J. Titus, R. Alonso Mori, M. L. Baker, D. A. Bennett, H.-M. Cho, W. B. Doriese, J. W. Fowler, K. J. Gaffney, A. Gallo, J. D. Gard, G. C. Hilton, H. Jang, Y. I. Joe, C. J. Kenney, J. Knight, T. Kroll, J.-S. Lee, D. Li, D. Lu, R. Marks, M. P. Minitti, K. M. Morgan, H. Ogasawara, G. C. O'Neil, C. D. Reintsema, D. R. Schmidt, D. Sokaras, J. N. Ullom, T.-C. Weng, C. Williams, B. A. Young, D. S. Swetz, K. D. Irwin, and D. Nordlund, "Soft x-ray spectroscopy with transition-edge sensors at Stanford Synchrotron Radiation Lightsource beamline 10-1," Rev. Sci. Instrum. **90**(11), 113101 (2019).

[16]P. Szypryt, G. C. O'Neil, E. Takacs, J. N. Tan, S. W. Buechele, A. S. Naing, D. A. Bennett, W. B. Doriese, M. Durkin, J. W. Fowler, J. D. Gard, G. C. Hilton, K. M. Morgan, C. D. Reintsema, D. R. Schmidt, D. S. Swetz, J. N. Ullom, and Y. Ralchenko, "A transition-edge sensor-based x-ray spectrometer for the study of highly charged ions at the National Institute Of Standards And Technology electron beam ion trap," Rev. Sci. Instrum. **90**(12), 123107 (2019).

[17]Y. Il Joe, Y. Fang, S. Lee, S. X. L. Sun, G. A. de la Peña, W. B. Doriese, K. M. Morgan, J. W. Fowler, L. R. Vale, F. Rodolakis, J. L. McChesney, J. N. Ullom, D. S. Swetz, and P. Abbamonte, "Resonant soft x-ray scattering from stripe-ordered $La_{2-x}Ba_xCuO_4$ detected by a transition-edge sensor array detector," Phys. Rev. Appl. **13**, 034026 (2020).

[18]M. R. J. Palosaari, M. Käyhkö, K. M. Kinnunen, M. Laitinen, J. Julin, J. Malm, T. Sajavaara, W. B. Doriese, J. Fowler, C. Reintsema, D. Swetz, D. Schmidt, J. N. Ullom, and I. J. Maasilta, "Broadband ultrahigh-resolution spectroscopy of particle-induced x rays: Extending the limits of nondestructive analysis," Phys. Rev. Appl. **6**, 024002 (2016).

[19]L. Miaja-Avila, G. C. O'Neil, Y. I. Joe, B. K. Alpert, N. H. Damrauer, W. B. Doriese, S. M. Fatur, J. W. Fowler, G. C. Hilton, R. Jimenez, C. D. Reintsema, D. R. Schmidt, K. L. Silverman, D. S. Swetz, H. Tatsuno, and J. N. Ullom, "Ultrafast time-resolved hard x-ray emission spectroscopy on a tabletop," Phys. Rev. X **6**, 031047 (2016).

[20]Y. Terada, S. Goto, N. Takimoto, K. Takeshita, H. Yamazaki, Y. Shimizu, S. Takahashi, H. Ohashi, Y. Furukawa, T. Matsushita, T. Ohata, Y. Ishizawa, T. Uruga, H. Kitamura, T. Ishikawa, and S. Hayakawa, "Construction and commissioning of Bl37XU at SPring-8," AIP Conf. Proc. **705**(1), 376–379 (2004).

[21]C. D. Reintsema, J. Beyer, S. W. Nam, S. Deiker, G. C. Hilton, K. Irwin, J. Martinis, J. Ullom, L. R. Vale, and M. Macintosh, "Prototype system for superconducting quantum interference device multiplexing of large-format transition-edge sensor arrays," Rev. Sci. Instrum. **74**(10), 4500–4508 (2003).

[22]A. E. Szymkowiak, R. L. Kelley, S. H. Moseley, and C. K. Stahle, "Signal processing for microcalorimeters," J. Low Temp. Phys. **93**(3-4), 281–285 (1993).

[23]J. W. Fowler, B. K. Alpert, W. B. Doriese, Y.-I. Joe, G. C. O'Neil, J. N. Ullom, and D. S. Swetz, "The practice of pulse processing," J. Low Temp. Phys. **184**(1), 374–381 (2016).

[24]S. Yamada, H. Tatsuno, S. Okada, and T. Hashimoto, "Coevolution of the technology on transition-edge-sensor spectrometer and its application to fundamental science," J. Low Temp. Phys. **200**, 418 (2020).

[25]G. Hölzer, M. Fritsch, M. Deutsch, J. Härtwig, and E. Förster, "$K\alpha_{1,2}$ and $K\beta_{1,3}$ x-ray emission lines of the 3d transition metals," Phys. Rev. A **56**(6), 4554–4568 (1997).

[26]H. Tatsuno, W. B. Doriese, D. A. Bennett, C. Curceanu, J. W. Fowler, J. Gard, F. P. Gustafsson, T. Hashimoto, R. S. Hayano, J. P. Hays-Wehle, G. C. Hilton, M. Iliescu, S. Ishimoto, K. Itahashi, M. Iwasaki, K. Kuwabara, Y. Ma, J. Marton, H. Noda, G. C. O'Neil, S. Okada, H. Outa, C. D. Reintsema, M. Sato, D. R. Schmidt, H. Shi, K. Suzuki, T. Suzuki, J. Uhlig, J. N. Ullom, E. Widmann, S. Yamada, J. Zmeskal, and D. S. Swetz, "Absolute energy calibration of x-ray $TES_S$ with 0.04 eV uncertainty at 6.4 keV in a hadron-beam environment," J. Low Temp. Phys. **184**(3), 930–937 (2016).

[27]D. Yan, R. Divan, L. M. Gades, P. Kenesei, T. J. Madden, A. Miceli, J.-S. Park, U. M. Patel, O. Quaranta, H. Sharma, D. A. Bennett, W. B. Doriese, J. W. Fowler, J. D. Gard, J. P. Hays-Wehle, K. M. Morgan, D. R. Schmidt, D. S. Swetz, and J. N. Ullom, "Eliminating the non-Gaussian spectral response of x-ray absorbers for transition-edge sensors," Appl. Phys. Lett. **111**(19), 192602 (2017).

[28]Y. Ishisaki, S. Yamada, H. Seta, M. S. Tashiro, S. Takeda, Y. Terada, Y. Kato, M. Tsujimoto, S. Koyama, K. Mitsuda, M. Sawada, K. R. Boyce, M. P. Chiao, T. Watanabe, M. A. Leutenegger, M. E. Eckart, F. S. Porter, and C. A. Kilbourne, "In-flight performance of pulse-processing system of the ASTRO-H/Hitomi soft x-ray spectrometer," J. Astron. Telesc. Instrum. Syst. **4**(1), 011217 (2018).

[29]B. Alpert, E. Ferri, D. Bennett, M. Faverzani, J. Fowler, A. Giachero, J. Hays-Wehle, M. Maino, A. Nucciotti, A. Puiu, D. Swetz, and J. Ullom, "Algorithms for identification of nearly-coincident events in calorimetric sensors," J. Low Temp. Phys. **184**(1), 263–273 (2016).

[30]M. E. Eckart, J. S. Adams, K. R. Boyce, G. V. Brown, M. P. Chiao, R. Fujimoto, D. Haas, J.-W. den Herder, A. Hoshino, Y. Ishisaki, C. A. Kilbourne, S. Kitamoto, M. A. Leutenegger, D. McCammon, K. Mitsuda, F. S. Porter, K. Sato, M. Sawada, H. Seta, G. A. Sneiderman, A. E. Szymkowiak, Y. Takei, M. S. Tashiro, M. Tsujimoto, C. P. de Vries, T. Watanabe, S. Yamada, and N. Y. Yamasaki, "Ground calibration of the ASTRO-H (Hitomi) soft x-ray spectrometer," J. Astron. Telesc. Instrum. Syst. **4**(2), 021406 (2018).

[31]H. Tatsuno, D. A. Bennett, W. B. Doriese, M. S. Durkin, J. W. Fowler, J. D. Gard, T. Hashimoto, R. Hayakawa, T. Hayashi, G. C. Hilton, Y. Ichinohe, H. Noda, G. C. O'Neil, S. Okada, C. D. Reintsema, D. R. Schmidt, D. S. Swetz, J. N. Ullom, S. Yamada, and the J-PARC E62 Collaboration, "Mitigating the effects of charged particle strikes on TES arrays for exotic atom x-ray experiments," J. Low Temp. Phys. **200**, 247 (2020).

[32]NIST SRM 610, Trace Elements in Glass, https://www-s.nist.gov/srmors/view_detail.cfm?srm=610, Certificate year, 2012.

[33]T. Schoonjans, A. Brunetti, B. Golosio, M. Sanchez del Rio, V. A. Solé, C. Ferrero, and L. Vincze, "The xraylib library for x-ray–matter interactions. recent developments," Spectrochim. Acta, Part B **66**(11), 776–784 (2011).

[34]B. K. Kuhn, K. Birbaum, Y. Luo, and D. Günther, "Fundamental studies on the ablation behaviour of Pb/U in NIST 610 and zircon 91500 using laser ablation inductively coupled plasma mass spectrometry with respect to geochronology," J. Anal. At. Spectrom. **25**, 21–27 (2010).

[35]F. Ana-Maria and D. Busselberg, "Occurrence, use and potential toxic effects of metals and metal compounds," BioMetals **19**(4), 332–336 (2006).

[36]J. R. Davenport and F. J. Peryea, "Phosphate fertilizers influence leaching of lead and arsenic in a soil contaminated with lead arsenate," Water, Air, Soil Pollut. **57-58**(1), 101–110 (1991).

[37]S. L. Brown, I. Clausen, M. A. Chappell, K. G. Scheckel, M. Newville, and G. M. Hettiarachchi, "High-iron biosolids compost–induced changes in lead and arsenic speciation and bioaccessibility in co-contaminated soils," J. Environ. Qual. **41**(5), 1612–1622 (2012).

[38]J. Liu and L. Luo, "Uptake and transport of Pb across the iron plaque of waterlogged dropwort (*Oenanthe javanica* DC.) based on micro-XRF and XANES," Plant Soil **441**(1), 191–205 (2019).
[39]D. M. Murphy, P. K. Hudson, D. J. Cziczo, S. Gallavardin, K. D. Froyd, M. V. Johnston, A. M. Middlebrook, M. S. Reinard, D. S. Thomson, T. Thornberry, and A. S. Wexler, "Distribution of lead in single atmospheric particles," Atmos. Chem. Phys. **7**(12), 3195–3210 (2007).
[40]S. R. Taylor and S. M. McLennan, *The Continental Crust: Its Composition and Evolution* (Black-well Publishers, Palo Alto, CA, USA, 1985).
[41]J. H. Martin and S. E. Fitzwater, "Iron deficiency limits phytoplankton growth in the north-east Pacific subarctic," Nature **331**(6154), 341–343 (1988).
[42]C. M. Moore, M. M. Mills, K. R. Arrigo, I. Berman-Frank, L. Bopp, P. W. Boyd, E. D. Galbraith, R. J. Geider, C. Guieu, S. L. Jaccard, T. D. Jickells, J. La Roche, T. M. Lenton, N. M. Mahowald, E. Marañón, I. Marinov, J. K. Moore, T. Nakatsuka, A. Oschlies, M. A. Saito, T. F. Thingstad, A. Tsuda, and O. Ulloa, "Processes and patterns of oceanic nutrient limitation," Nat. Geosci. **6**(9), 701–710 (2013).
[43]T. D. Jickells, Z. S. An, K. K. Andersen, A. R. Baker, G. Bergametti, N. Brooks, J. J. Cao, P. W. Boyd, R. A. Duce, K. A. Hunter, H. Kawahata, N. Kubilay, J. laRoche, P. S. Liss, N. Mahowald, J. M. Prospero, A. J. Ridgwell, I. Tegen, and R. Torres, "Global iron connections between desert dust, ocean biogeochemistry, and climate," Science **308**(5718), 67–71 (2005).
[44]M. Kurisu, K. Sakata, C. Miyamoto, Y. Takaku, T. Iizuka, and Y. Takahashi, "Variation of iron isotope ratios in anthropogenic materials emitted through combustion processes," Chem. Lett. **45**(8), 970–972 (2016).
[45]A. R. Baker, W. M. Landing, E. Bucciarelli, M. Cheize, S. Fietz, C. T. Hayes, D. Kadko, P. L. Morton, N. Rogan, G. Sarthou, R. U. Shelley, Z. Shi, A. Shiller, and M. M. P. van Hulten, "Trace element and isotope deposition across the air 2013; sea interface: Progress and research needs," Philos. Trans. R. Soc., A **374**(2081), 20160190 (2016).
[46]E. R. Sholkovitz, P. N. Sedwick, and T. M. Church, "Influence of anthropogenic combustion emissions on the deposition of soluble aerosol iron to the ocean: Empirical estimates for island sites in the north atlantic," Geochim. Cosmochim. Acta **73**(14), 3981–4003 (2009).
[47]A. W. Schroth, J. Crusius, E. R. Sholkovitz, and B. C. Bostick, "Iron solubility driven by speciation in dust sources to the ocean," Nat. Geosci. **2**(5), 337–340 (2009).
[48]Y. Takahashi, T. Furukawa, Y. Kanai, M. Uematsu, G. Zheng, and M. A. Marcus, "Seasonal changes in Fe species and soluble Fe concentration in the atmosphere in the Northwest Pacific region based on the analysis of aerosols collected in Tsukuba, Japan," Atmos. Chem. Phys. **13**(15), 7695–7710 (2013).
[49]M. Kurisu, K. Adachi, K. Sakata, and Y. Takahashi, "Stable isotope ratios of combustion iron produced by evaporation in a steel plant," ACS Earth Space Chem. **3**(4), 588–598 (2019).
[50]K. Sakata, M. Kurisu, H. Tanimoto, A. Sakaguchi, M. Uematsu, C. Miyamoto, and Y. Takahashi, "Custom-made PtFe filters for ultra-clean size-fractionated aerosol sampling for trace metals," Mar. Chem. **206**, 100–108 (2018).
[51]S. Yamada, M. Axelsson, Y. Ishisaki, S. Konami, N. Takemura, R. L. Kelley, C. A. Kilbourne, M. A. Leutenegger, F. S. Porter, M. E. Eckart, and A. Szymkowiak, "Poisson vs. Gaussian statistics for sparse x-ray data: Application to the soft x-ray spectrometer," Publ. Astron. Soc. Jpn. **71**(4), 75 (2019).
[52]J. Kawai, M. Ohta, and T. Konishi, "Chemical effects in high-resolution nickel Kalpha x-ray fluorescence spectra," Anal. Sci. **21**(7), 865–868 (2005).
[53]H. Hayashi, "Lifetime-broadening-suppressed selective XAFS spectroscopy," Anal. Sci. **24**(1), 15–23 (2008).
[54]A. C. Thompson and D. Vaughan, Center for X-ray Optics, Lawrence Berkeley National Laboratory, Center for X-Ray Optics, Advanced Light Source, and Lawrence Berkeley National Laboratory, Advanced Light Source, X-Ray Data Booklet, Lawrence Berkeley National Laboratory, University of California, 2001.
[55]J. A. B. Mates, D. T. Becker, D. A. Bennett, B. J. Dober, J. D. Gard, J. P. Hays-Wehle, J. W. Fowler, G. C. Hilton, C. D. Reintsema, D. R. Schmidt, D. S. Swetz, L. R. Vale, and J. N. Ullom, "Simultaneous readout of 128 x-ray and gamma-ray transition-edge microcalorimeters using microwave SQUID multiplexing," Appl. Phys. Lett. **111**(6), 062601 (2017).
[56]W. Yoon, J. S. Adams, S. R. Bandler, D. Becker, D. A. Bennett, J. A. Chervenak, A. M. Datesman, M. E. Eckart, F. M. Finkbeiner, J. W. Fowler, J. D. Gard, G. C. Hilton, R. L. Kelley, C. A. Kilbourne, J. A. B. Mates, A. R. Miniussi, S. H. Moseley, O. Noroozian, F. S. Porter, C. D. Reintsema, J. E. Sadleir, K. Sakai, S. J. Smith, T. R. Stevenson, D. S. Swetz, J. N. Ullom, L. R. Vale, N. A. Wakeham, E. J. Wassell, and E. J. Wollack, "Toward large field-of-view high-resolution x-ray imaging spectrometers: Microwave multiplexed readout of 28 TES microcalorimeters," J. Low Temp. Phys. **193**(3), 258–266 (2018).
[57]K. Sakai, J. S. Adams, S. R. Bandler, D. A. Bennett, K. D. Irwin, and J. A. B. Mates, "Development of space-flight compatible room-temperature electronics for the Lynx x-ray microcalorimeter," J. Astron. Telesc. Instrum. Syst. **5**(2), 021013 (2019).
[58]E. Boydaş, E. Orhan, M. G. Boydaş, and E. Cömert, "Chemical shifts of kα and $k\beta_{1,3}$ x-ray emission spectra for oxygen compounds of Ti, Cr, Fe, Co, Cu with WDXRF," in *World Conference on Technology, Innovation and Entrepreneurship* [Procedia **195**, 1757–1761 (2015)].